ISPRS Journal of Photogrammetry and Remote Sensing 180 (2021) 238–254

Contents lists available at ScienceDirect

ISPRS Journal of Photogrammetry and Remote Sensing

journal homepage: www.elsevier.com/locate/isprsjprs

Global clear sky near-surface imagery from multiple satellite daily imagery time series

Karlis Mikelsons [a,b,*], Menghua Wang [a]

[a] NOAA National Environmental Satellite, Data, and Information Service, Center for Satellite Applications and Research, E/RA3, 5830 University Research Court, College Park, MD 20740, USA
[b] Global Science and Technology, Inc., Greenbelt, MD 20770, USA

ARTICLE INFO

Keywords:
Remote sensing
Surface feature
True color
False color
VIIRS
Sentinel-3 OLCI
Landsat

ABSTRACT

We develop a new statistically-robust adaptive regression method (SARM) to extract clear sky true color imagery, approximating the near-surface imagery, derived from multiple satellite daily imagery time series, while avoiding artifacts due to clouds and cloud shadows. We compare the SARM-derived near-surface imagery against simpler approaches for various surface types, and perform a quantitative evaluation. Existing mapped daily imagery from the Visible Infrared Imaging Radiometer Suite (VIIRS) onboard the Suomi National Polar-orbiting Partnership (SNPP) and NOAA-20, and the Ocean and Land Colour Instrument (OLCI) on the Sentinel-3A and Sentinel-3B satellites is used to produce global clear sky near-surface imagery over various time intervals. We provide several examples of satellite-derived clear sky near-surface imagery over various regions to show potential applications. In addition, we apply this new method to derive clear sky near-surface imagery using higher spatial resolution Landsat-8 data, and discuss characteristics and limitations of our approach. The clear sky near-surface imagery is a useful satellite-derived product, representing the human perception of Earth's near-surface features, which can be more directly interpreted and easily understood by the general public, and aids visualization and interpretation of various types of satellite derived data.

1. Introduction

In recent years, we have seen rapid growth of Earth observations from space, including environmental monitoring and imaging of land and ocean surface, atmosphere, and cryosphere. Most of the global environment monitoring and imaging sensors fly in polar low-Earth sun-synchronous orbits, and some satellites achieve complete global coverage every day. For example, the Visible Infrared Imaging Radiometer Suite (VIIRS) on the Suomi National Polar-orbiting Partnership (SNPP) and NOAA-20 satellites perform radiometric measurements at 22 spectral bands from the visible to the near-infrared (NIR), the shortwave infrared (SWIR), and thermal infrared with spatial resolution ranging from 375 m to 750 m, and can achieve complete daily global coverage (Goldberg et al., 2013). The Ocean and Land Colour Instrument (OLCI) on the Sentinel-3A and Sentinel-3B satellites measures reflectance at 21 visible, NIR, and SWIR spectral bands with 300 m spatial resolution, and reaches complete global coverage in ~3–4 days (Donlon et al., 2012). Higher spatial resolution imagery sensors typically have fewer spectral bands and lower revisit frequency due to narrower swath width, and usually only perform measurements over land and coastal areas. For example, the Operational Land Imager (OLI) onboard the Landsat-8 satellite measures nine visible and infrared bands at 15–30 m spatial resolution, and a 16-day revisit interval (Roy et al., 2014). Constellations of commercial satellite imagers may achieve even higher spatial resolution daily global coverage, e.g., PlanetScope miniature satellite (CubeSat) data with spatial resolution in meters (https://www.planet.com/products/planet-imagery/).

One of the simplest and most intuitive types of satellite-derived data is true color imagery, which attempts to portray Earth's appearance as seen by human vision (near above Earth's surface or near the cloud top), and only requires measurements in three visible bands. While true color imagery can only provide a qualitative overview of Earth's surface, it is commonly used in combination with many environmental data products to aid visualization. The global daily true color imagery from VIIRS-SNPP, VIIRS-NOAA-20, and OLCI-Sentinel-3A/3B sensors is routinely produced by NOAA Ocean Color Team and displayed in the Ocean Color

* Corresponding author at: NOAA National Environmental Satellite, Data, and Information Service, Center for Satellite Applications and Research, E/RA3, 5830 University Research Court, College Park, MD 20740, USA.
E-mail address: Karlis.Mikelsons@noaa.gov (K. Mikelsons).

https://doi.org/10.1016/j.isprsjprs.2021.08.013
Received 17 February 2021; Received in revised form 28 June 2021; Accepted 13 August 2021
Available online 28 August 2021
0924-2716/© 2021 The Authors. Published by Elsevier B.V. on behalf of International Society for Photogrammetry and Remote Sensing, Inc. (ISPRS). This is an open access article under the CC BY license (http://creativecommons.org/licenses/by/4.0/).

Viewer (OCView) (Mikelsons and Wang, 2018), along with many global ocean color data product imageries, e.g., normalized water-leaving radiance spectra $nL_w(\lambda)$ (IOCCG, 2010; Wang et al., 2013b), chlorophyll-a concentration (Hu et al., 2012; O'Reilly and Werdell, 2019; Wang and Son, 2016), water diffuse attenuation coefficient at 490 nm $K_d(490)$ (Wang et al., 2009), water inherent optical properties (IOPs) (Lee et al., 2002; Shi and Wang, 2019), etc. NASA WorldView (worldview.earthdata.nasa.gov) also provides imagery and various environmental data from VIIRS SNPP and NOAA-20, and from the Moderate Resolution Imaging Spectroradiometer (MODIS) (Salomonson et al., 1989) on the Terra and Aqua satellites.

Most of Earth's surface at any moment is covered by clouds (King et al., 2013). For the purposes of land and ocean surface (or top layer) property studies, it is desirable to avoid clouds (i.e., cloud masking) (Ackerman et al., 1998; Wang and Shi, 2006), but also mask out smoke and heavy dust in the atmosphere. Thus, cloud detection and masking in satellite imagery becomes of paramount importance and many approaches have been developed to address it. Most of the cloud detection methods rely on physical properties reflected in multispectral imagery (Scaramuzza et al., 2012; Zhu et al., 2015; Zhu and Woodcock, 2012), while some have used spatial context (Hughes and Hayes, 2014). Over waters, satellite measurements are also often impacted by specular reflection off the water surface (sun glint) (Cox and Munk, 1954; Wang and Bailey, 2001). In general, cloud detection is a complex problem. Depending on the application, various degrees of thin clouds, or partial cloud shadows may be permissible. For example, even thin clouds, or close proximity of the observed area to bright clouds typically degrade or prohibit ocean color retrievals (Jiang and Wang, 2013; Mikelsons et al., 2020). Yet the impact on the imagery data is usually less severe. In fact, the presence of thin clouds or moderate aerosols may only partially obscure the surface, and even measurements of areas under cloud shadow may also provide some useful information about the surface appearance.

Indeed, several methods have been developed to remove thin clouds from satellite imagery using the spectral information and spatial correlations. Hu et al. (2015) used wavelet transform spatial filtering to remove thin clouds from satellite imagery. Xu et al. (2019) developed a method to remove thin clouds from Landsat imagery using multiple spectral bands. However, such methods are limited to either relatively thin, or small and sparse clouds. In general, removal of large thick clouds requires multiple observations.

While the changes in the atmosphere (such as cloud cover and distribution) are often occurring on relatively short time scales (hours), changes in water surface usually have longer time scales, with exceptions for coastal waters, e.g., impacted by the tidal variation (Shi et al., 2011, 2013). Changes over land are typically even more gradual. These most commonly involve seasonal changes of vegetation (Beurs and Henebry, 2004; Defries and Townshend, 2007), as well as snow and ice cover.

A wide variety of multi-temporal techniques have been developed for cloud detection (Frantz et al., 2015; Zhu and Woodcock, 2012), as well as for the reconstruction of the cloud obscured areas, including local linear and non-linear predictors (Benabdelkader and Melgani, 2008; Melgani, 2006), local neighborhood similar pixel interpolation (Zhu et al., 2012), spatial and temporal regression methods (Chen et al., 2017; Gómez-Chova et al., 2017; Mateo-Garcia et al., 2018), information cloning (Lin et al., 2013), and deep convolutional neural network algorithms (Zhang et al., 2020; Zhang et al., 2018), and combinations of methods (Zhang et al., 2021). Other approaches have focused on deriving a representative global imagery by extending the multi-temporal series to longer time intervals. For example, Sentinel-2 satellite imageries from years 2017–2018 have been combined to produce the global cloud free land surface imagery (Corbane et al., 2020). Yearly Sentinel-2 global clear sky imagery has also been derived by EOX IT Services GmbH and is freely available (https://s2maps.eu/). However, some boundaries between adjacent orbits are noticeable.

In addition to satellite imagery, a wide range of techniques based on temporal and spatial data aggregation and filtering have also been employed to improve the data coverage and quality for many different types of measurements over the ocean (Chen et al., 2019; Liu and Wang, 2019; Stock et al., 2020) and land (Sharma et al., 2017).

Since multi-temporal techniques for deriving clear sky imagery require time series of geo-co-located imagery, the data availability and computational cost become significant factors (Mateo-Garcia et al., 2018), especially when global clear sky imagery is desired. However, daily global true color imagery is readily available from Terra and Aqua MODIS (NASA WorldView; worldview.earthdata.nasa.gov), SNPP and NOAA-20 VIIRS, and Sentinel 3A/B OLCI (Mikelsons and Wang, 2018), covering multiple years. In addition, the true color imagery is already corrected for Rayleigh scattering in the atmosphere, which eliminates another computational expense.

In this study, we aim to take advantage of the existing true color global daily imagery archives for multiple satellite sensors, and to derive the global clear sky imagery for various time intervals. We show how to combine true color imagery from multiple partially cloudy scenes and derive a statistically robust estimate for the darkest clear sky sample, at the same time minimizing the effects of cloud shadows. In order to avoid any biases and artifacts, we do not use any previous knowledge, or any imagery outside the specified time interval. The resultant imagery minimizes atmospheric effects (e.g., cloud cover, cloud shadows, heavy aerosols, etc.), as well as sun glint over water and snow and ice cover. Since the resultant imagery is derived using a number of input images, it is not a mosaic of individual scenes and does not show boundaries or discontinuities characteristic to mosaic imagery.

The paper is structured as follows: we introduce and describe the details of our method in Section 2, and provide the results for evaluation and list several applications in Section 3. We discuss the results in Section 4 before concluding in Section 5.

2. Methodology

2.1. Production of daily true color imagery

The daily imagery used in this study is derived from satellite-measured radiances at three visible bands corresponding to human perception of blue, green, and red colors, for each of the four sensors (two VIIRS and two OLCI). The particular selection of spectral bands used are listed in Table 1. The top-of-atmosphere (TOA) reflectances measured by each sensor are corrected for Rayleigh scattering radiance contributions, producing the Rayleigh-corrected reflectances at the three visible bands (blue, green, and red), which are then mapped onto the image RGB values (each band/channel value ranging from 0 to 255). We use a non-linear enhancement to emphasize the darker land and water surfaces at the expense of less contrast for brighter clouds. Thus, the RGB values in the image are not directly proportional to the actual

Table 1
Nominal center wavelengths of the bands used to derive the true color imagery.

Sensor	Blue		Green		Red		Sharpening	
	Band	λ (nm)	Band	λ (nm)	Band	λ (nm)	Band	λ (nm)
VIIRS-SNPP	M3	486	M4	551	M5	671	I1	638
VIIRS-NOAA-20	M3	489	M4	556	M5	667	I1	642
OLCI-Sentinel-3A/3B	4	490	6	560	8	665	–	–
OLI-Landsat-8	2	482	3	561	4	655	8	589

band reflectances. The band nominal center wavelengths differ slightly among different sensors (see Table 1), but are overall fairly close (especially for qualitative or visual comparison). We note that it is not always practical to store information on corrected reflectances, whereas true color imagery takes much less space due to fewer radiometric discrete levels and thus can be better compressed.

In order to compare and analyze the imagery recorded by multiple satellite sensors at different times, it has to be mapped in the same spatial projection using the same spatial resolution. We use the geographical projection for most of our global studies, and polar stereographic projections for a better representation of the Arctic and Antarctic polar areas. For each sensor, the daily imagery from multiple orbits is merged based on smaller sensor-zenith angle (or a combination of solar-zenith and sensor-zenith angles for imagery in polar stereographic projections). While the medium resolution bands of VIIRS have spatial resolution of about 750 m, we use VIIRS imagery band (I1; see Table 1) to enhance it to 375 m. The visible bands of OLCI sensors have a spatial resolution of about 300 m. Therefore, we use the sampling resolution of about 300 m from VIIRS and OLCI for the global imagery in the geographical projection. In fact, the daily imagery from these four sensors is routinely produced and displayed in OCView (Mikelsons and Wang, 2018).

Thus, we use a series of mapped true color images from several satellite sensors covering a range of time, and aim to produce a single image that minimizes cloud cover, eliminates spectral differences among the sensors, and reduces any noise or inconsistencies that may arise due to compositing multiple images from different sensors.

2.2. The darkest sample method (DSM)

While many of the methods for cloud identification use spatial filtering to infer the information about the particular location, in this work, we perform entirely local analysis based on the information from the same location (pixel) acquired on different times. That allows us to make no assumptions about the spatial correlations of surface reflectances, which avoid any problems in areas with sharp spatial changes in surface reflectance (such as coastal areas). The question is then reduced to finding the best estimate for the clear sky near-surface color, given a series of multiple daily scenes from multiple satellite sensors.

In the RGB space, each sample i out of the n total samples can be represented by the three-color channels: R_i, G_i, and B_i. To start with, we calculate the sum the three-color channels:

$$a(R,G,B) = R + G + B, \tag{1}$$

and call this quantity brightness. We then sort all the samples according to the increasing values of brightness. We first discard all samples with brightness exactly zero, as these represent areas within the image with no data. This happens in locations under polar night, due to missing data, or for pixels that are out of swath width in OLCI daily imagery. The remaining darkest samples contain the most information about the land or water surface, while the brightest samples are usually due to white clouds, snow, or ice.

One very simple and naïve approach is to form the clear sky near-surface image by choosing the darkest sample for each pixel from the input image series. We call this the "darkest sample method" (DSM). In general, however, this approach is very prone to artifacts from cloud and terrain shadows, as will be shown in many examples below. A much better, and more statistically robust estimate of the clear sky near-surface color can be obtained by using a number of the darkest samples.

2.3. The adaptive fraction method (AFM)

To identify the samples with the most information about the clear sky near-surface spectrum, we calculate the color saturation for each sample, defined as

$$S = [max(R,G,B) - min(R,G,B)]/max(R,G,B) \tag{2}$$

where max(R, G, B) and min(R, G, B) are the maximum and minimum of the three-color (R, G, B) values for each sample out of different input images. While there may be some fluctuations in the color saturation S due to different sensors and acquisition conditions, generally the color saturation S will sharply decrease to zero once the area becomes obscured by clouds. We use that fact to select the number of the lowest brightness samples to use in the further analysis. For that, we define integrated color saturation:

$$\Sigma(a) = \int_0^a S(a')da'. \tag{3}$$

The rationale behind using this quantity is that samples with relatively large saturation S, which are spread over a range of brightness values a, constitute the useful information. We choose the number of the darkest samples m such that

$$\Sigma(a_m) = f_a \Sigma(a_n), \tag{4}$$

where a_n is the brightness of the nth darkest pixel, and factor f_a is an adjustable parameter, chosen to be close to, but less than 1. The idea is to reject the brightest samples with small values of color saturation. Obviously, choosing $f_a = 1$ implies that $m = n$, and therefore it is not a useful choice. Choosing f_a slightly less than 1 results in selecting $m < n$ samples with larger color saturation and discarding the rest. While the results are not very sensitive to the exact value of parameter f_a, we find that $f_a = 0.9$ works well. We show the results of the parameter sensitivity analysis in the Supplementary material (see Section S1).

However, in some cases, such as for snow or ice surface, this approach results in only a few selected samples. Therefore, we ensure that at least the minimum number of samples $n_{min} = 10$ is selected, in order to retain enough information for statistical analysis and to avoid spurious noisy behavior due to small number of samples. To account for the cases where the number of the original samples n is less than 10, we set $n_{min} = min(n, 10)$. At the same time, we also limit the maximum number of samples to be less than $n_{max} = 100$, mostly for the reasons of computational efficiency, because further increases have little effect on the results. This condition only affects analysis over extended time periods. Thus, after these adjustments, we select number of the darkest samples for further analysis as

$$n_s = min[n_{max}, max(n_{min}, m)], \tag{5}$$

where m is the number of the darkest samples defined in Eq. (4). The rest of $n - n_s$ samples are discarded.

At this point, we formulate another simple, yet improved approach whereby to derive the clear sky near-surface imagery: the values of three-color channels are calculated as the median values over the darkest n_s samples for each channel. We call this method the "adaptive fraction method" (AFM). This approach is clearly more statistically robust than DSM, and it mostly avoids the artifacts due to cloud shadows. However, as will be shown later, the resultant imagery is also often contaminated with remnants of clouds. Therefore, we seek to further improve it by exploiting additional information contained in the series of samples.

2.4. Analysis of saturation for different surface types

To help visualize this process of sample selection, and to gain a better understanding on how the color saturation depends on the brightness for different types of Earth's surface, we show the dependence of saturation on the brightness for six distinct surface types in Fig. 1. We have selected three distinct land surface types (forest, desert, and ice), and three distinct water surface types (open ocean, shallow water, and sediment-

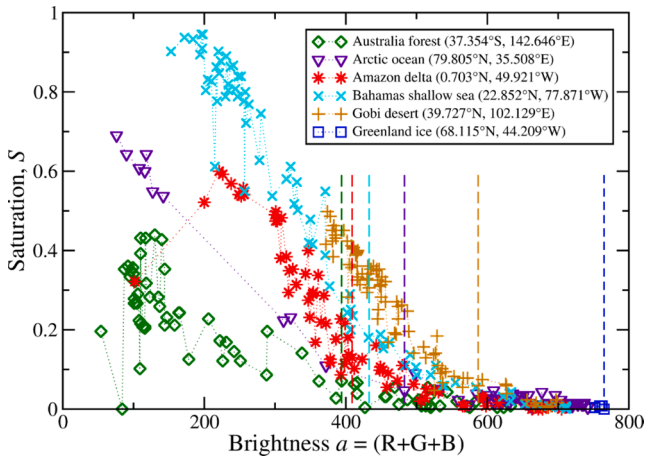

Fig. 1. Color saturation S versus brightness for the six distinct land and water surface types. Cloud contamination generally increases brightness, while decreasing the color saturation. The dashed vertical lines represent the cutoff values used to select the darkest samples used in further analysis. Data were obtained from VIIRS and OLCI true color imageries in May 2020.

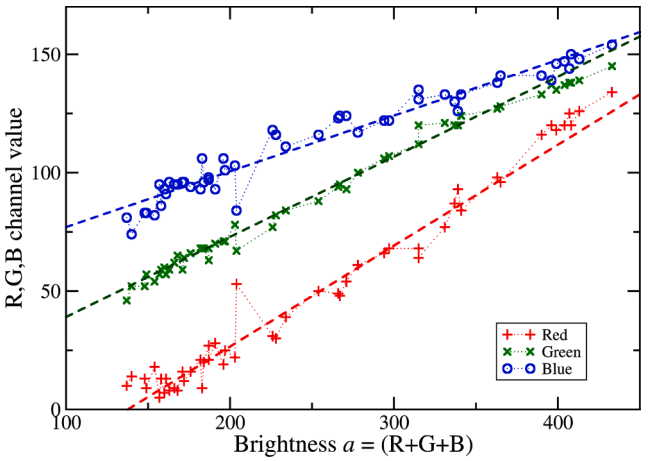

Fig. 2. Values of the three-color channels plotted versus brightness showing a typical linear inter-dependence of the three R, G, and B values. The dashed lines show the Theil-Sen linear fits. Data were obtained from VIIRS and OLCI true color imageries in May 2020 for shallow water in the Great Bahama Bank at (22.852°N, 77.871°W).

rich water). Of course, these six cases do not cover the wide variety of different surface types and conditions, but are just merely a minimal representative set of cases for the purposes of illustration. In general, saturation decreases with increasing brightness. The cutoff values of brightness corresponding to the darkest samples selected for further analysis are displayed as vertical dashed lines. These cutoff values strongly depend on the surface properties and observation conditions for each location.

The locations, coordinates, and the cutoff values a_m, as well as the number of selected samples n_s for each location are summarized in Table 2.

2.5. The proposed statistically-robust adaptive regression method (SARM)

In this section, we introduce and provide the details of the proposed SARM method. As the name suggests, it employs a statistically robust regression to model linear correlations in the input data samples. An adaptive procedure based on correlations between the sample color saturation and brightness is then used to estimate the darkest sample free of clouds or cloud shadows.

We note that the values of the three-color channels for the selected darkest samples are linearly correlated. As an example, in Fig. 2, we display the values of R, G, and B channels versus their sum (brightness). The values of the three-color channels taken from different scenes with various cloud coverage are linearly dependent on the brightness. We can use this fact to improve the estimation of the clear sky near-surface color, thus further decreasing the impact of the clouds.

However, instead of using a least-squares fit versus brightness for each of the three-color channels separately, we use a Theil-Sen estimate to calculate the slope (Sen, 1968; Theil, 1950). This involves calculating the median of all the slopes between every pair of input samples for each channel. Thus, the slope for the red channel is

$$\beta_R = median\left[\frac{R_i - R_j}{a_i - a_j}\right](0 < j < i \le n_s), \tag{6}$$

where R_i, and R_j are the values of the red channel for samples i and j, respectively, and a_i and a_j are the corresponding values of brightness for these samples. We use similar expressions for the green and blue bands. The advantage of this approach is that it is statistically robust and less impacted by outliers. The values of slopes $(\beta_R, \beta_G, \beta_B)$ represent a statistically robust estimate for the direction associated with the principal component of samples in the three-dimensional RGB space. Next, we calculate the median values of the offsets $(\alpha_R, \alpha_G, \alpha_B)$. However, instead of calculating the offsets in RGB space, we do that in a transformed coordinate system where one of the axes is aligned with the estimate for the principal direction. Thus, we transform all data (R, G, B) triplets to a coordinate system where one of the axes is aligned with our robust estimate for the slopes $(\beta_R, \beta_G, \beta_B)$. We then find the median values along each coordinate direction and transform the median values back to the original (R, G, B) space to yield the three offset values $(\alpha_R, \alpha_G, \alpha_B)$. The resultant linear fit is given by a parametric line equation:

$$\frac{R - \alpha_R}{\beta_R} = \frac{G - \alpha_G}{\beta_G} = \frac{B - \alpha_B}{\beta_B} = d. \tag{7}$$

Here, the parameter d determines the position on the line in the three-dimensional (R, G, B) space. Finding this line equation is somewhat similar to finding the largest principal component of a set of sample points in the RGB space with the advantage of statistical robustness.

At this point, we only need to determine the optimal value of the parameter d to use for the estimate of the clear sky near-surface color. First, we note that choosing $d = 0$ is somewhat equivalent to the

Table 2
Sample locations of distinct surface types in Fig. 1, along with the cutoff values a_m and number of samples n_s used in subsequent statistical analysis for each case.

Sample location	Coordinates	Surface type	a_m	n_s
Australia, New South Wales	37.354°S, 142.646°E	Forest, austral winter	394	48
Arctic Ocean	79.805°N, 35.508°E	Open ocean, ice patches	483	10
Amazon River Delta	0.703°N, 49.921°W	Sediment rich water	409	28
Great Bahama Bank	22.852°N, 77.871°W	Clear shallow water	433	45
Gobi Desert	39.727°N, 102.129°E	Desert, frequent clouds	587	75
Greenland	68.115°N, 44.209°W	Polar ice cap	765	10

approach of AFM, because it involves calculating the median values over all pre-selected samples, although in a transformed coordinate space. Second, we note that the minimum (and maximum) possible values for parameter d are set by a condition that the values of all three-color channels have to be in the range from 0 to 255. Thus, we can write

$$d_{min} = max\left[-\frac{\alpha_R}{\beta_R}, -\frac{\alpha_G}{\beta_G}, -\frac{\alpha_B}{\beta_B}\right], \text{ and} \tag{8}$$

$$d_{max} = min\left[\frac{255-\alpha_R}{\beta_R}, \frac{255-\alpha_G}{\beta_G}, \frac{255-\alpha_B}{\beta_B}\right] \tag{9}$$

Overall, lower values of d will minimize the effects of cloud contamination. However, choosing $d = d_{min}$ results in too dark and completely saturated color. Another possibility is to select the value of d corresponding to the darkest pixel, but that is strongly sensitive to outlier values. Instead, we attempt a somewhat ad hoc approach to obtain a more robust estimate based on the distribution of points along the principal direction. We project the (R, G, B) values of each sample onto the line of the principal direction, and record the positions d_i for each sample i. Due to samples being sorted in the order of increasing brightness, the position d_i is overall increasing with sample number (see Fig. 3a). We again use a Theil-Sen estimate to find the slope of $d_i(i)$, and then find an estimate for the intercept d_{fit} as median of all residual values. We further enforce that d_{fit} is not less than d_{min}, i.e., $d_{fit} = max(d_{fit}, d_{min})$. This is an improvement towards clearer, less cloudy imagery. However, in many cases it will still be affected by the effects of cloud shadow, thus adding more noise in the resultant image.

In order to understand how to minimize the effects of cloud shadows, we look at how the color saturation depends on the brightness value for different scenes. On the one hand, if we choose a set of samples that are not affected by cloud shadows, then the color saturation increases the darker pixel gets (less cloud cover means more saturated surface color). On the other hand, if the color saturation decreases with decreasing brightness, that is an indicator that some of the samples are affected by cloud shadows. These two distinct scenarios are illustrated in Fig. 3b. This observation can be used to adaptively adjust the value of parameter d to avoid the effects of cloud shadows in a following way: we calculate the correlation between the color saturation S_i and the position on the principal axis d_i over all selected samples, i.e., $c = corr(S_i, d_i)$. Then, if the S_i and d_i are perfectly anti-correlated ($c = -1$), we choose $d = d_{fit}$, whereas for a perfect positive correlation ($c = 1$), we choose $d = 0$. For any values in between, we choose $d = d_{fit}(1-c)/2$. We note that this approach also helps to minimize shadows from terrain and buildings, which is more important in higher spatial resolution imagery. However, input imagery over longer time periods (seasons) may be necessary to completely remove terrain and building shadows. Finally, we use the adjusted value for parameter d to calculate the estimates for clear sky near-surface color as:

$$\begin{cases} R = \alpha_R + \beta_R d \\ G = \alpha_G + \beta_G d \\ B = \alpha_B + \beta_B d \end{cases} \tag{10}$$

The entire procedure is repeated for each pixel to produce a complete clear sky near-surface image from a series of daily scenes from multiple satellite sensors.

3. Results

3.1. Evaluation and validation

3.1.1. Visual evaluation and comparison

To demonstrate the advantages of the proposed SARM to derive the clear sky near-surface imagery, we compare it with the results from two simpler methods described previously: the approaches of DSM and AFM. We compare the derived clear sky near-surface imagery for three distinct types of land surface in Fig. 4. In all three cases, the clear sky near-surface imagery is derived from the daily true color imageries from measurements of the two VIIRS and two OLCI sensors in May 2020. In the first case, it shows arid land in the Gobi Desert, Mongolia (Fig. 4a–c). The DSM imagery (Fig. 4a) is severely contaminated by cloud shadows and practically unusable. The AFM (Fig. 4b) produces significantly better results. However, the results by our proposed SARM in Fig. 4c not only eliminate the artifacts of cloud shadows, but also improve the contrast compared to AFM image in Fig. 4b.

In the second case (Fig. 4d–f), it shows the Andes Mountains in Colombia, which are frequently covered with clouds. The DSM (Fig. 4d) minimizes the cloud cover, but also illustrates that some locations may be persistently covered by clouds for the entire month. As in Fig. 4a, the DSM results are contaminated by cloud shadows (some highlighted with red boxes). The results from the AFM (Fig. 4e) show significant cloud contamination for this scene, while avoiding the effects of cloud shadows. The new SARM (Fig. 4f) shows only slightly more cloudy areas than the DSM image in Fig. 4d, but it mostly eliminates the effects of cloud shadows elsewhere.

In the third case (Fig. 4g–i), shows forest and farmland in Victoria, Australia. Again, the DSM results (Fig. 4g) are severely affected by cloud shadows. The AFM avoids the cloud shadow effects (Fig. 4h), but the new SARM (Fig. 4i) provides a further slight improvement in the image contrast.

We also show comparisons of the three methods for various types of coastal water surface in Fig. 5. The first scene (Fig. 5a–c) shows the Great Bahama Bank, a vast expanse of clear and shallow water. The DSM results (Fig. 5a) again suffer from severe cloud shadow contamination (highlighted by red boxes in the upper part of the image). The AFM

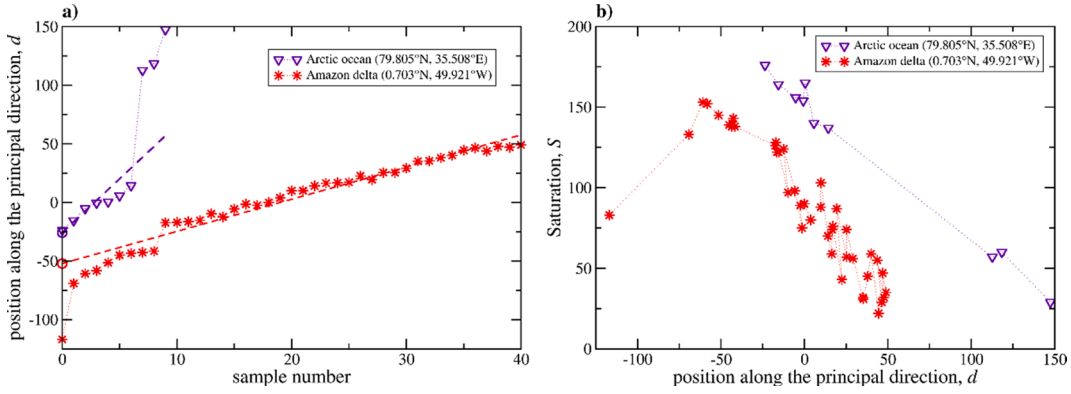

Fig. 3. (a) The distribution of samples along the principal direction. The dashed lines indicate the linear Theil-Sen fits used to obtain a robust estimate of the lowest position along the principal direction as the intercept d_{fit} (shown as circles). (b) Dependence of color saturation on sample position along the principal direction. Data were obtained from VIIRS and OLCI true color imageries in May 2020.

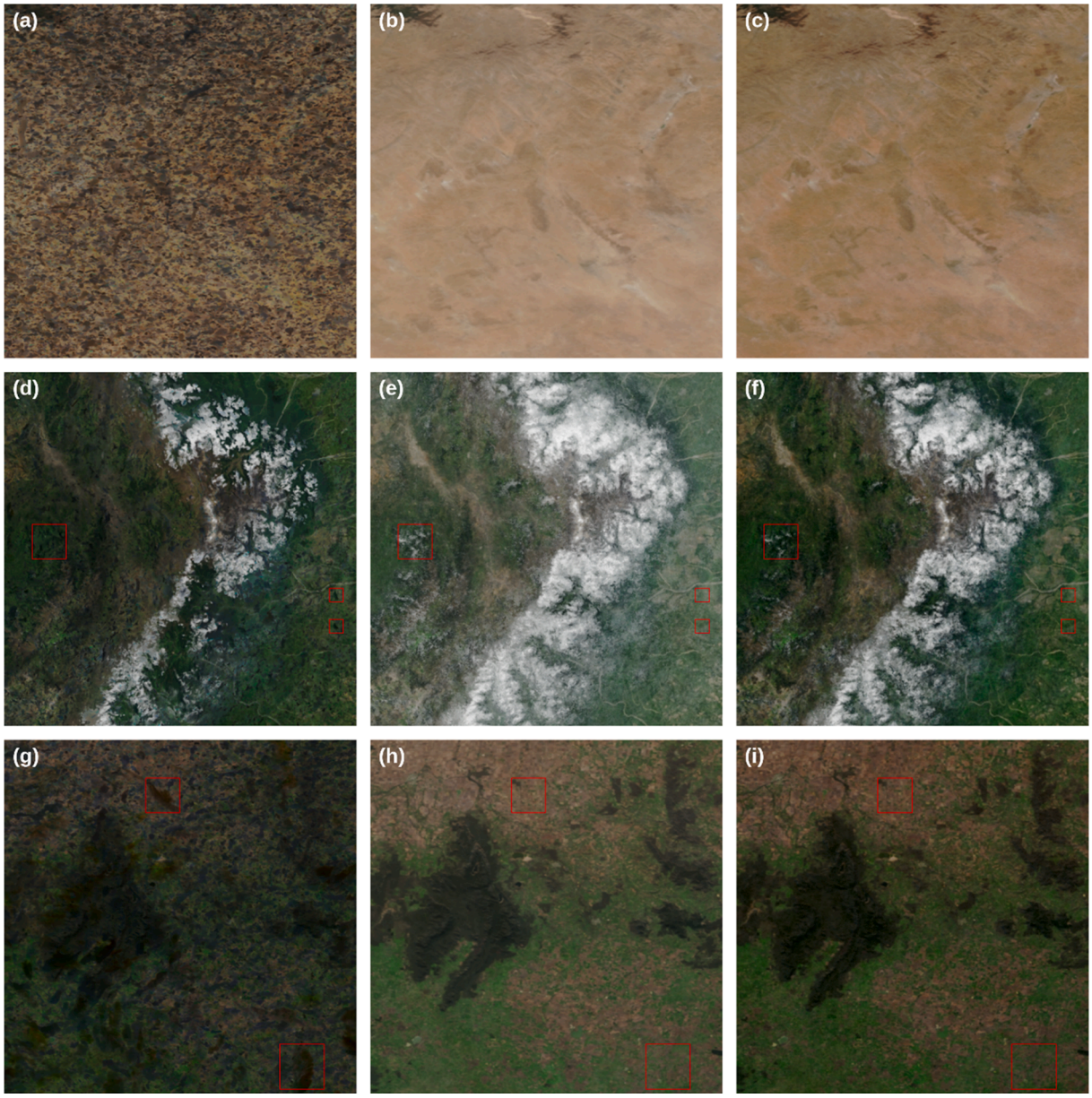

Fig. 4. Comparison of three methods for clear sky near-surface imagery over three types of land surface: left column (a, d, g)–DSM; center column (b, e, h)–AFM; right column (c, f, i)–the new SARM. Scene identification: (a–c): Gobi Desert, Mongolia (47.1°N, 107.6°E); (d–f): Andes, Colombia (6.3°N, 72.4°W); (g–i) Victoria, Australia (37.3°S, 142.7°E). All images were derived using VIIRS and OLCI daily imageries in May 2020. Some obvious differences are highlighted with red boxes. (For interpretation of the references to color in this figure legend, the reader is referred to the web version of this article.)

offers a significantly improved, good quality image (Fig. 5b), but some cloud contamination is evident (highlighted by the box in lower part of the image). Our new SARM (Fig. 5c) shows a further slight improvement in image contrast over the AFM result.

The second scene features the Amazon River Estuary with light brown sediment-rich waters, and vegetation covered land (Fig. 5d–f). Results from the DSM again display cloud shadow effects both over land and water (Fig. 5d). The approach of AFM eliminates cloud shadows (Fig. 5e), but some cloud contamination is still evident, especially over land. The new SARM (Fig. 5f) produces a good contrast image without either type of artifact.

In the last example, we show icy Arctic waters near the East Greenland Coast (Fig. 5g–i). Here, the DSM works reasonably well (Fig. 5g), partly due to less frequent cloud shadows in this area, and partly due to the effects of the cloud shadows being less noticeable over the dark Arctic waters. In addition to removing clouds, it also removes most of the transient sea ice. Results from the AFM (Fig. 5h), however, show significantly more cloud and ice contamination. The new SARM (Fig. 5i) is able to avoid clouds and ice almost to the same extent as that from the DSM (Fig. 5g).

As seen from the examples in Figs. 4 and 5, the new SARM combines the advantages of both the DSM and AFM, while mostly avoiding the drawbacks of both methods.

3.1.2. *Quantitative evaluations*

We also perform a quantitative evaluation of SARM, and compare the results with the simpler DSM and AFM methods. We choose a region around the Great Salt Lake, Utah, USA for evaluation, as it covers a relatively wide range of land and water surface types. We use the daily imagery from SNPP and NOAA-20 sensors from two days (August 14 and September 1, 2020; see Fig. 6) with perfectly clear skies to generate a reference image. As seen in Fig. 6, there are some minor changes to the

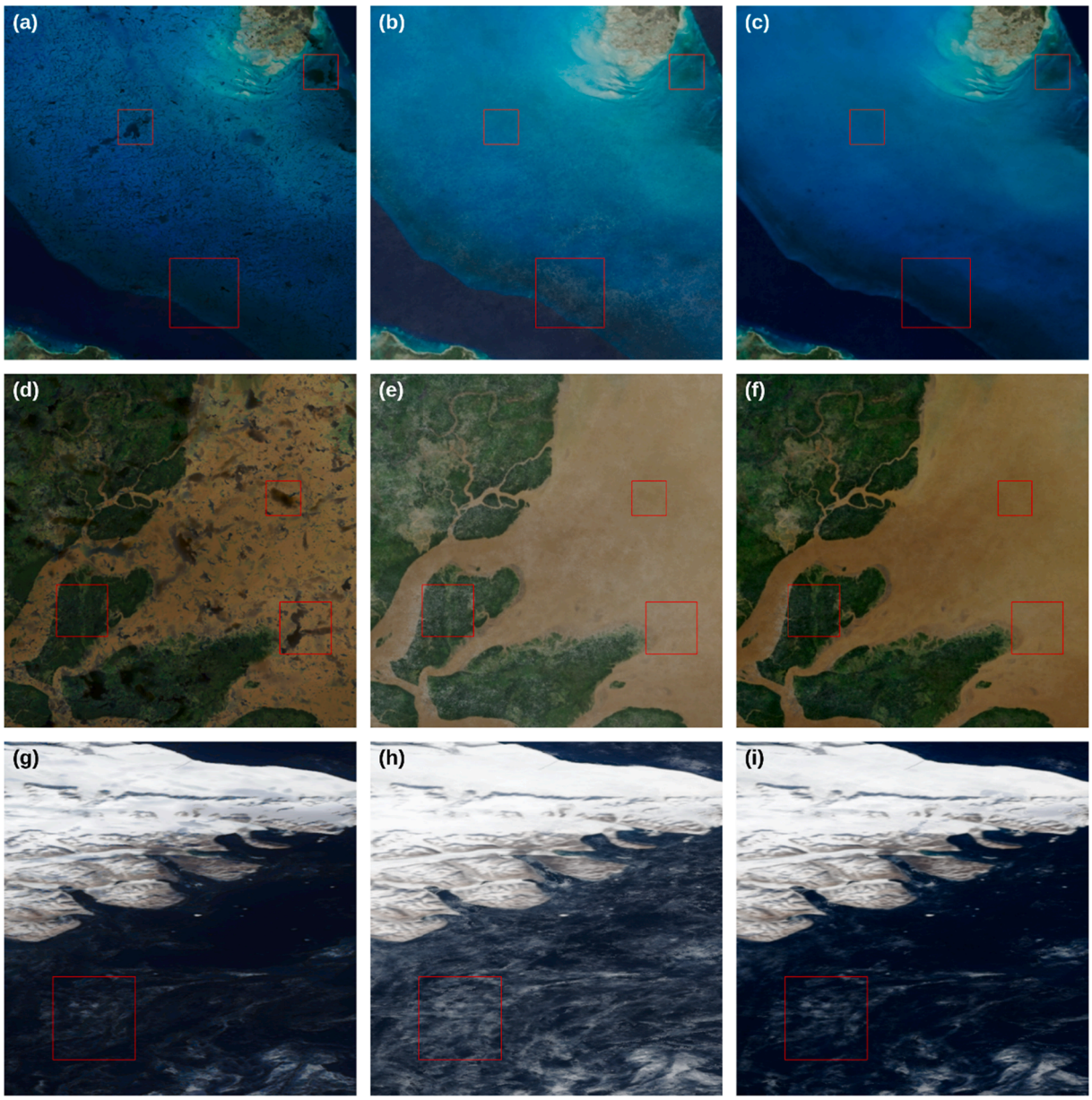

Fig. 5. Comparison of three methods for clear sky near-surface imagery over coastal areas: left column (a, d, g)–DSM; center column (b, e, h)–AFM; right column (c, f, i)–the new SARM. Scene identification: (a–c): the Great Bahama Bank (23.2°N, 78W°E); (d–f): the Amazon River Estuary (0.7°N, 50°W); (g–i) the East Greenland Coast (69.6°N, 23.2°W). All images were derived using VIIRS and OLCI daily imageries in May 2020. Some obvious differences are highlighted with red boxes. (For interpretation of the references to color in this figure legend, the reader is referred to the web version of this article.)

land and water surface during this time period. Also, some differences are noticeable between the same day imagery from the two sensors due to slight changes to the retrieval conditions (such as sensor-solar geometry). For these reasons, we use the average over the four scenes in Fig. 6 as a representative reference of clear sky image for the selected time period and spatial area (shown in Fig. 8d).

We then select a series of nine consecutive days from August 18–26, 2020, which have moderate to severe cloud presence in the chosen location in both VIIRS-SNPP and VIIRS-NOAA-20 imagery. The daily imagery from VIIRS-SNPP for these nine days is shown in Fig. 7. The corresponding VIIRS-NOAA-20 daily imagery has a very similar cloud cover. However, the clouds may be shifted due to the ~50 min time interval between the observations from the two sensors.

Thus, we use 18 cloudy daily scenes from two sensors over a nine-day period to derive the clear sky imagery with the DSM, AFM, and SARM methods. The comparison of the results is shown in Fig. 8. As expected, DSM imagery (Fig. 8a) is severely contaminated by cloud shadows, while the AFM-derived imagery (Fig. 8b) lacks contrast due to remnants of clouds. The SARM results (Fig. 8c) are significantly better and quite comparable to the reference image (Fig. 8d) obtained as an average over the clear sky daily scenes.

The reference image can be considered as the “ground truth,” and used to quantitatively evaluate the clear sky imagery. We use the root mean square difference (RMSD) from the reference image, calculated over the entire image and the three-color channels, to evaluate the results from DSM, AFM, and SARM. We also calculate the RMSD for the daily imagery for both sensors, including the clear days used to produce the reference image. These results are shown in Table 3.

The four scenes from the two clear days show that the variation of the clear sky due to land water and surface changes, as well as changes to the satellite retrieval geometry, is about 10 units. This is very close to the difference of SARM derived clear sky imagery over the period of nine

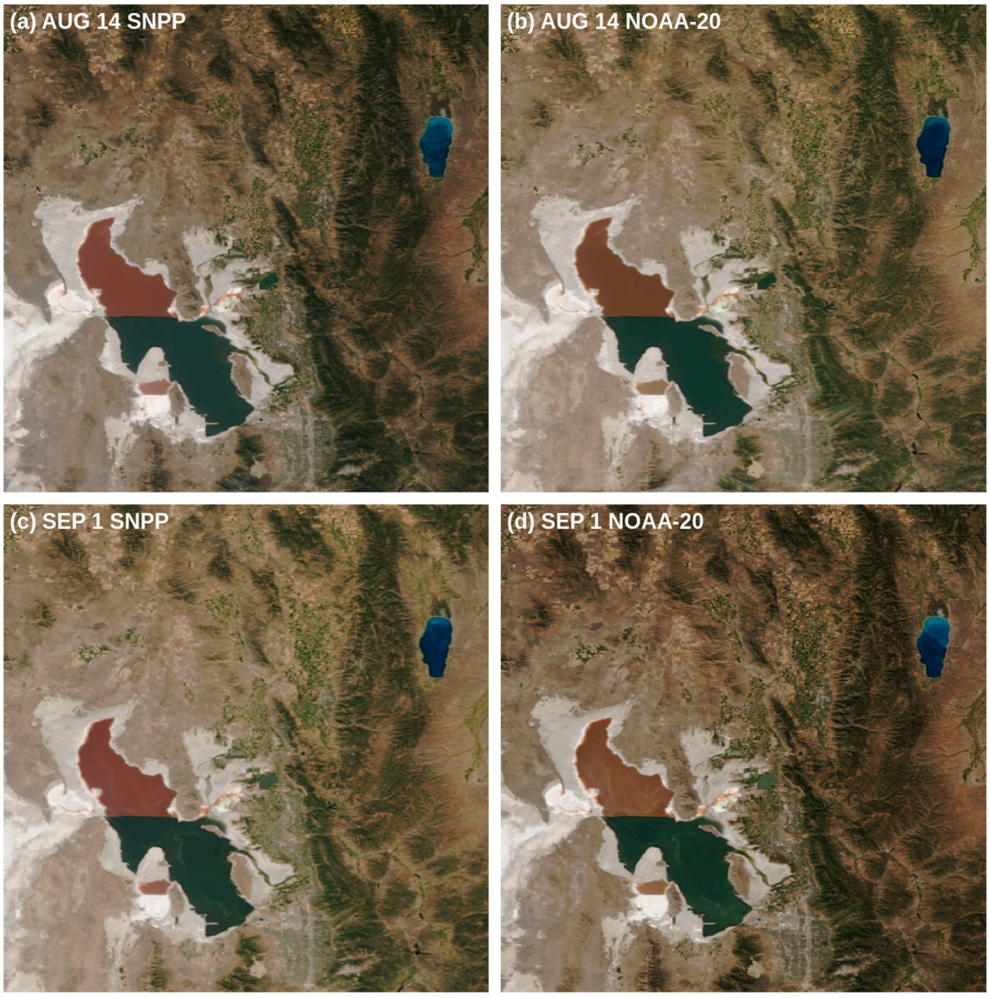

Fig. 6. Daily clear sky imagery for the area surrounding the Great Salt Lake from VIIRS-SNPP (a and c) and VIIRS-NOAA-20 (b and d) for August 14, 2020 (a and b), and September 1, 2020 (c and d). Slight differences among the four scenes are due to land/water surface changes and changes in satellite retrieval conditions. The average of the four scenes is shown as the reference image in Fig. 8d.

cloudy days. However, the RMSD for DSM and AFM results is twice as large. Scatter plots comparing the reference image and the DSM, AFM, and SARM results (Fig. 9) also confirm that SARM recovers the overall pixel value distribution of the reference image in each of the color channels, whereas DSM tends to underestimate the reflectance due to the cloud shadow contamination, and AFM overestimates the reflectance due to the cloud contamination. We conclude that SARM produces clear sky imagery that is consistent (both visually and statistically) with the corresponding daily complete clear sky imagery.

3.1.3. *Quantitative evaluations over global water surface*

We also perform a much wider quantitative evaluation of SARM results over the global water surface using the cloud mask information obtained from the ocean color retrievals. The ocean color retrieval process produces a set of flags indicating a number of conditions affecting the retrievals, such as cloud cover (Ackerman et al., 1998; Wang and Shi, 2006), cloud shadows and straylight (Jiang and Wang, 2013), heavy aerosol presence, medium or high sun glint (Cox and Munk, 1954; Wang and Bailey, 2001), and floating ice. We use this set of flags as a rigorous cloud mask over water surface. For each pixel in the true color imagery, we find the corresponding set of the ocean color flags, and exclude that pixel from any further analysis if the flags indicate any of the aforementioned conditions. We also exclude any land pixels in the step. Then, we collect the masked true color imagery over a certain time period, and use the mean and the minimum values in these time series to compare with the results from SARM derived for the same time period. We note that since the masked imagery excludes cloud shadows, using the minimum value in the time series provides a reasonable estimate. We also note that despite aggregation over time, the masked imagery may still have gaps in over water surface, which we exclude from comparison with SARM results. We use the mean difference (MD or bias) and RMSD to quantify the difference over the two sets of imagery. In contrast to the reference imagery, the SARM results were derived using only the daily global imagery over the same time period, but without any additional information about clouds or cloud shadows. The results are shown in Table 4 for monthly and 8-day time intervals, for the two methods (the minimum and mean values) of calculating the reference imagery. We use only VIIRS SNPP and NOAA-20 imagery in this comparison.

As seen in the Table 4, the RMSD between the SARM results and the reference imagery obtained by using the ocean color data mask is comparable to the example shown in Fig. 8 and Table 3. We note that we get a better correspondence when using the minimum value of masked imagery time series in a comparison, especially for the average difference or bias. This may be because the mean values in the time series could include some pixels under slight sun glint conditions. Also, SARM is designed to produce the darkest naturally occurring pixel, which is what the minimum value in the time series represents. Overall, the vast extent of this comparison over the global water surface provides a significant quantitative test for the SARM results.

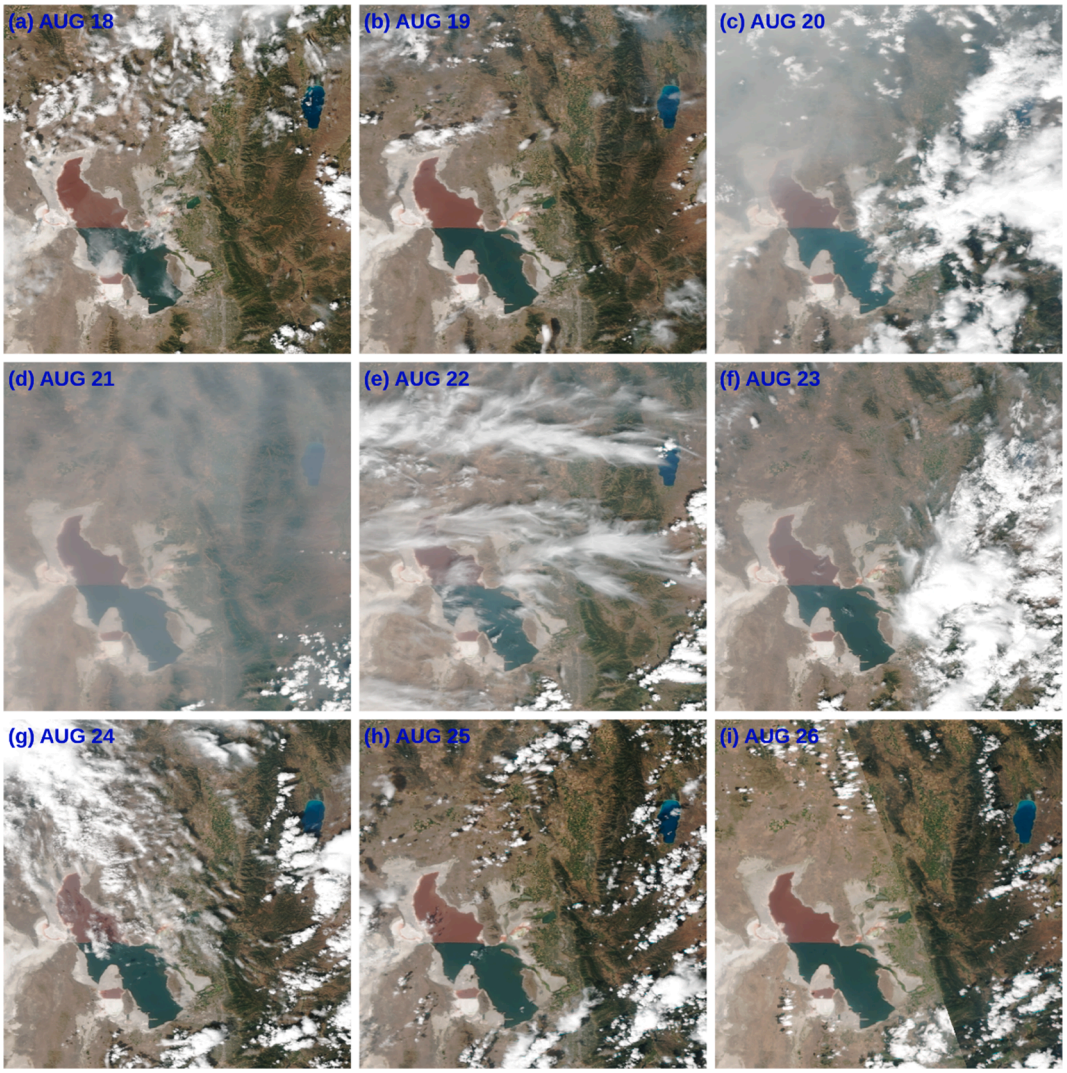

Fig. 7. Daily VIIRS-SNPP imagery for the area surrounding the Great Salt Lake for a nine-day period of August 18–26, 2020, showing a moderate to severe cloud and cloud shadow presence. The corresponding VIIRS-NOAA-20 imagery shows similar levels of cloud cover.

3.2. Comparison of different time averages

The quality of the derived clear sky near-surface imagery and the extent to which the clouds can be removed depends strongly on the number of daily scenes used in the analysis. When more daily scenes over longer time periods are used to derive the clear sky near-surface imagery, the fraction of image affected by clouds decreases. Due to high geographic variability of cloud frequency, the improvements in clear sky near-surface imagery are also quite location dependent. To illustrate the improvement of the quality of cloud free imagery with longer time periods used in the analysis, we show a comparison of global cloud free imagery derived over various time periods in Fig. 10. Fig. 10a shows the daily global true color imagery from VIIRS-SNPP. Similar daily coverage is derived from VIIRS-NOAA-20. The two OLCI instruments aboard Sentinel-3A/3B satellites have a narrower swath resulting in gaps of coverage of adjacent orbits. Data from all four sensors are used to derive the clear sky near-surface imagery. Fig. 10b shows the global clear sky near-surface imagery derived daily scenes over eight days, with a significant reduction of the cloud cover. However, many locations are still obscured by clouds due to persistent weather patterns. Similarly, Fig. 10c shows the monthly clear sky near-surface imagery for September 2019 with further reduction of cloudy areas. Lastly, Fig. 10d shows the global clear sky near-surface imagery derived from the entire year (2019) of daily imagery. The yearly clear sky near-surface imagery practically eliminates any clouds, but also shows the minimum extent of snow and ice coverage in both Arctic and Antarctic polar regions and mountain ranges. In addition, the clear sky algorithm favors the darker imagery of green vegetation over the lighter yellow–brown dried out land scenes in the areas that experience distinct wet and dry seasons. We note that at very large spatial and temporal scales the task of deriving the clear sky imagery becomes significantly easier, since more data samples are available, and various methods may yield comparable and good results (see, for example, NASA Blue Marble Imagery, https://visibleearth.nasa.gov/images/57752/blue-marble-land-surface-shallow-water-and-shaded-topography).

3.3. Global seasonal change

We show the seasonal change in global imagery in Fig. 11 using the proposed SARM. Here, we use the three-month long-time intervals to derive the global imagery representative of each of the four seasons with SARM. Fig. 11a shows boreal spring (March–May 2019) with large parts of the Northern Hemisphere still covered in snow/ice. In Fig. 11b (June–August 2019), the seasonal vegetation in the the Northern Hemisphere has reached the maximum extent. Fig. 11c (September–November 2019) shows fall colors in the Northern Hemisphere and

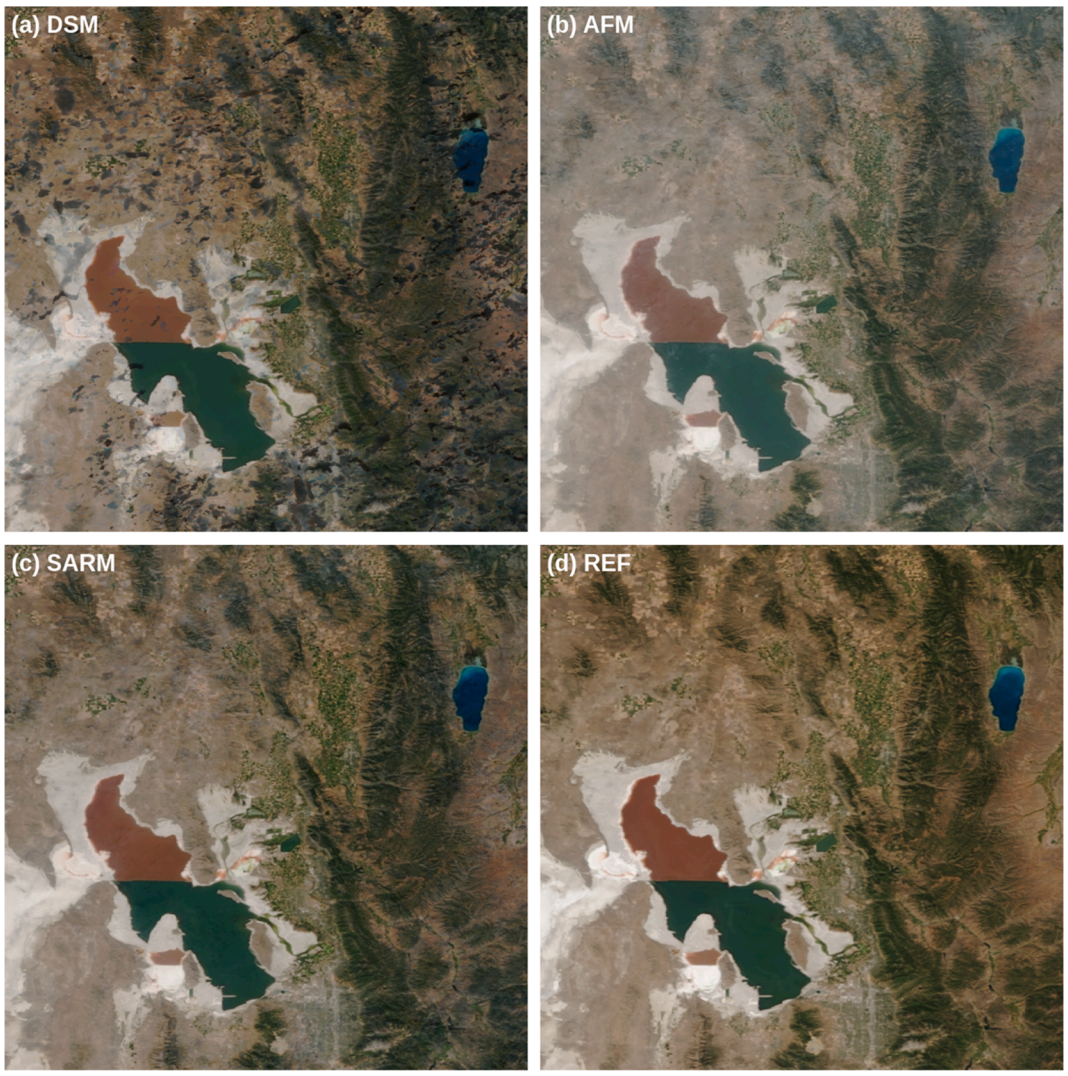

Fig. 8. Comparison of the clear sky imagery produced by (a) DSM, (b) AFM, and (c) SARM, as well as from (d) the reference image. The DSM results are contaminated by cloud shadows, while the AFM results show cloud contamination. The SARM imagery is clear of either type of artifacts and is comparable with the reference image.

Table 3
RMSD for the daily VIIRS SNPP and NOAA-20 imagery, as well as for the clear sky imagery derived by DSM, AFM, and SARM over the time period August 18–26, 2020. The units of RMSD are the same as the digital numbers corresponding to 8-bit color channels, ranging from 0 to 255.

Date	Satellite (VIIRS)		Algorithm		
	SNPP	NOAA-20	DSM	AFM	SARM
8/14[†]	10.9	9.7	–	–	–
8/18	51.4	50.0	–	–	–
8/19	29.7	36.2	–	–	–
8/20	92.5	60.8	–	–	–
8/21	55.7	36.8	–	–	–
8/22	69.9	55.3	20.8[‡]	20.9[‡]	10.0[‡]
8/23	84.9	95.6	–	–	–
8/24	70.5	87.6	–	–	–
8/25	50.8	64.6	–	–	–
8/26	42.4	35.6	–	–	–
9/1[†]	12.5	12.1	–	–	–

[†] Dates used to calculate the reference clear sky image.
[‡] The algorithm results represent the time period of August 18–26, 2020.

retreating ice around Antarctica. During the boreal winter (Fig. 11d, December 2019–February 2020), most of the land in northern latitudes was covered by snow/ice, while the sea ice around Antarctica had reached its minimum. We note that clear sky near-surface imagery cannot be derived if the daily imagery is absent for extended time periods due to polar night, such as for Antarctic and Arctic regions in Fig. 11b and 11d, respectively.

3.4. Changes over shorter time periods

The clear sky near-surface imagery can also be used to analyze various phenomena taking place over shorter time scales. In Fig. 12, we use the 8-day clear sky near-surface imagery to show the evolution of algae blooms in the North Sea in summer of 2020. Since this area is very frequently overcast, it is usually not possible to find a daily imagery with clear skies. In the 8-day clear sky near-surface imagery, however, only very small patches of cloudy areas remain (mostly over land). Yet at the same time, the 8-day time interval is still short enough to be able to capture the dynamics of various stages of the algae blooms.

In the polar areas, the clear sky near-surface imagery not only avoids the cloudy scenes, but it also shows the minimum extent of the snow and ice over the land and water surface. To illustrate this, we show monthly clear sky near-surface imagery over the Canadian arctic and west

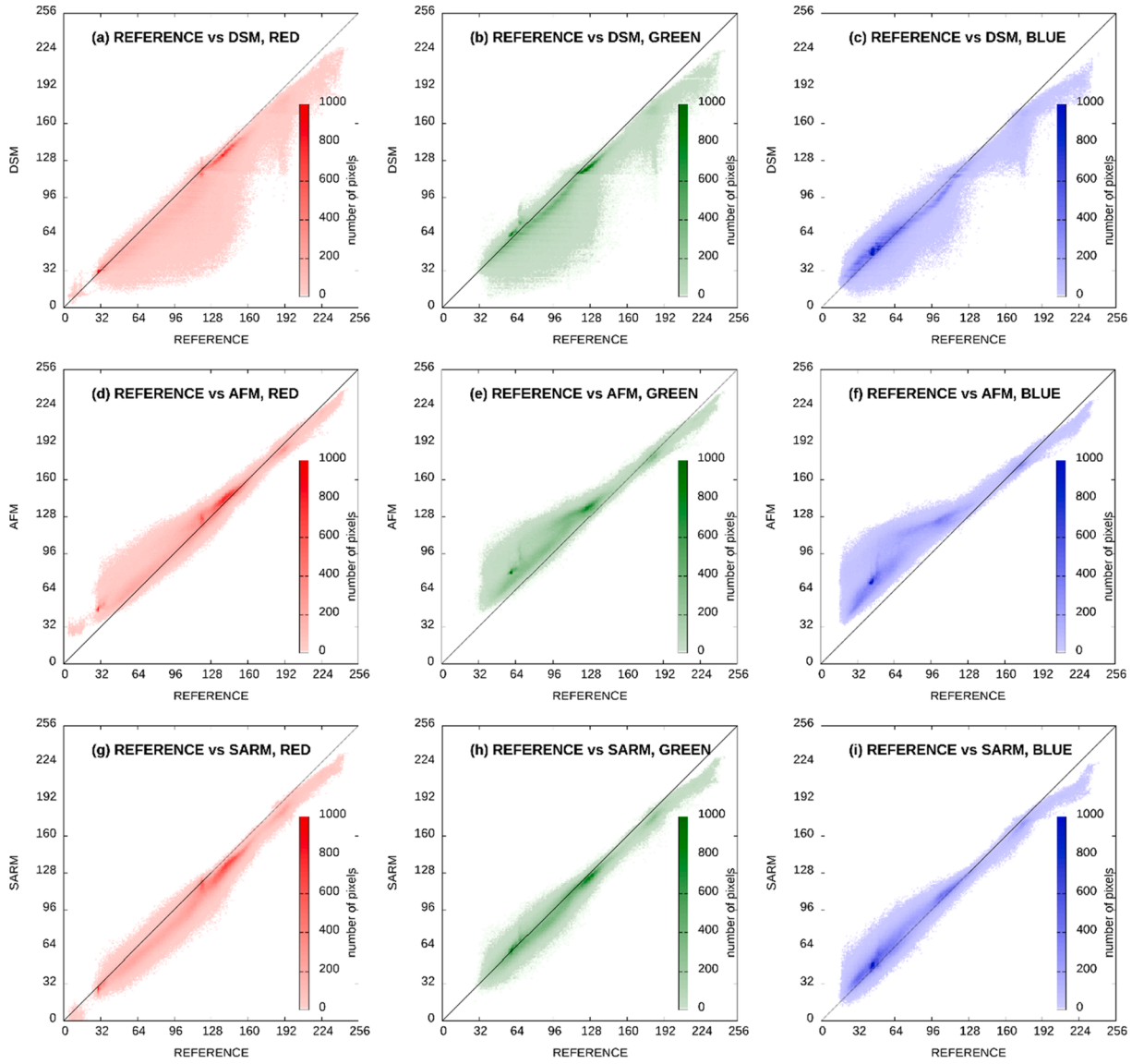

Fig. 9. Scatter plots of pixel comparison between the reference image (Fig. 8d), and DSM image in Fig. 8a (panels a–c), AFM image in Fig. 8b (panels d–f), and SARM results in Fig. 8c (panels g–i) in the three-color channels.

Table 4
Comparison of SARM imagery over global water surface with the reference imagery obtained by using ocean color data masks, for 8-day and monthly time intervals in 2020, using the minimum and mean values to calculate the reference imagery. The units of bias and RMSD are the same as the digital numbers corresponding to the 8-bit color channels, ranging from 0 to 255.

Time Interval	Reference Method			
	Minimum		Mean	
	Bias	RMSD	Bias	RMSD
September 1–30	1.7	7.8	11.7	13.6
September 5–12	3.4	11.1	8.9	13.9
September 13–20	3.7	11.0	9.4	14.1
September 21–28	3.1	11.6	9.1	14.6

Greenland region for four months during summer 2019 in Fig. 13. In June 2019 (Fig. 13a), the Northwest Passage (indicated by the red ellipse in Fig. 13), as well as most other channels in the archipelago were covered by solid ice. Similarly, most inland lakes were still frozen. In July 2019 (Fig. 13b), the ice in Baffin Bay and in most inland lakes had completely melted. In August 2019 (Fig. 13c), the sea ice in the northwest passage was breaking up, and in September 2019 (Fig. 13d), only patchy ice remained in the Northwest Passage. In fact, from the results in Fig. 13, we can see that the September 2019 image represented the minimum extent of the sea ice over the year 2019.

We have demonstrated several applications of the clear sky near-surface imagery, which corresponds to human color perception. However, the same methodology (i.e., SARM) can also be applied to various types of sky false color imagery derived using different combinations of spectral bands. One commonly used type of false color imagery is obtained by substituting the NIR band (865 nm) for the green band in the true color imagery. The vegetation is highly reflective in the NIR band resulting in bright green false color imagery, while water nearly completely absorbs in the NIR band, thus appears in purple color (Qi et al., 2020). This change of bands has little effect on the appearance of clouds, which are still white and brighter than land surface. This type of false color imagery is commonly used to monitor the changes in vegetation and the surface water extent. As an illustrative example, we show the changes to the surface waters in the northeast part of Bangladesh over the course of the year in Fig. 14. In the first panel (Fig. 14a), it shows the region in April 2019, and most of the area was covered by vegetation, with few rivers and lakes. By July 2019 (Fig. 14b), about one

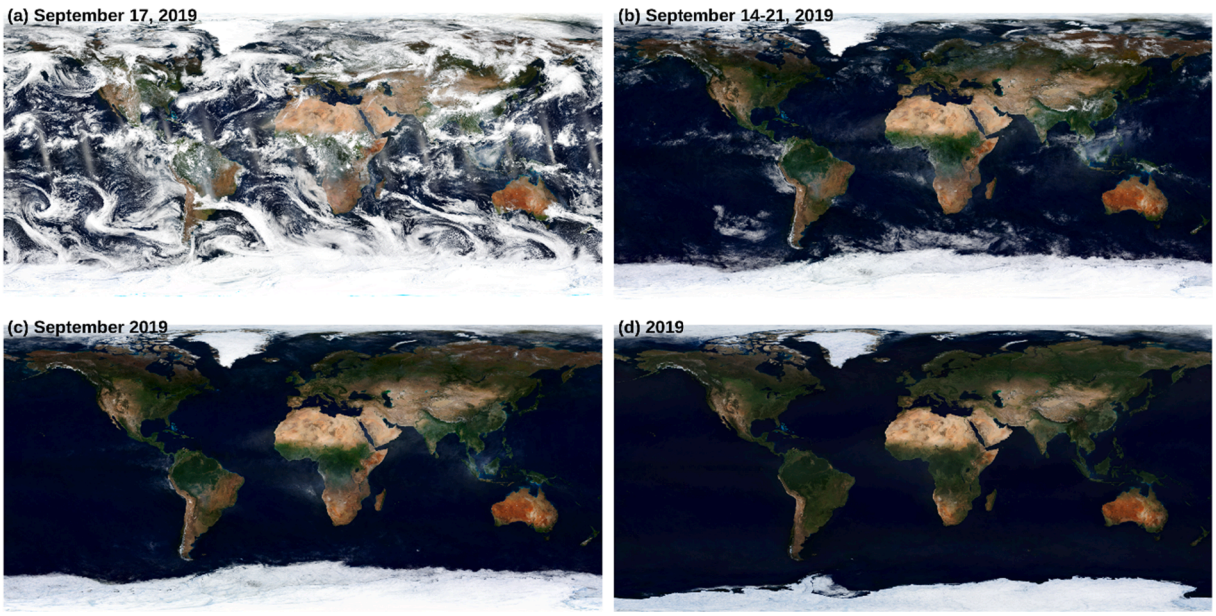

Fig. 10. Comparison of (a) daily VIIRS-SNPP global imagery on September 17, 2019, with the clear sky near-surface imagery derived from the daily global VIIRS-SNPP, VIIRS-NOAA-20, OLCI-Sentinel-3A, and OLCI-Sentinel-3B imageries over (b) 8-day (September 14–21, 2019), (c) monthly (September 2019), and (d) year-long (2019) time periods.

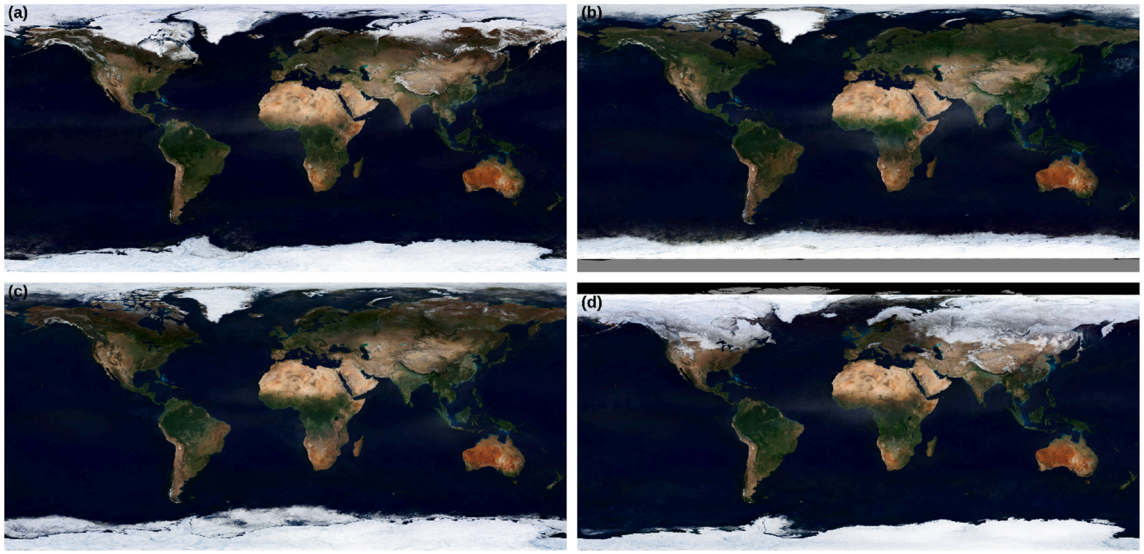

Fig. 11. Global clear sky near-surface imagery derived using the proposed SARM from the daily global VIIRS-SNPP, VIIRS-NOAA-20, OLCI-Sentinel-3A, and OLCI-Sentinel-3B imageries for the four seasons with 3-month time periods of (a) March–May 2019, (b) June–August 2019, (c) September–November 2019, and (d) December 2019–February 2020. Note that clear sky near-surface imagery cannot be derived for the areas under polar night in panels (b) and (d).

third of the approximately 150 × 150 km^2 area was covered by water. We note that due to persistent monsoon rains, this area is most frequently covered by clouds in July. However, the monthly clear sky near-surface imagery showed only few remnants of clouds in the northern part of the scene. Three months later, in October 2019 (Fig. 14c), the water still covered a significant fraction of the area. Lastly, by January 2020 (Fig. 14d), the water had receded and most of the area was again covered by vegetation. We note that since water generally appears darker in the false color imagery as compared to land or vegetation, it is somewhat favored in the derived clear sky false color images.

3.5. *Landsat-8 imagery*

Finally, since SARM makes no assumptions about the spatial resolution of the input imagery, it can be readily applied to derive clear sky near-surface imagery from other higher spatial resolution sensor data, such as Landsat-8 OLI. To demonstrate this, we have selected a location in Colombia, around the town of Pasto, where mountainous terrain results in very frequently overcast skies. Since higher spatial resolution Landsat-8 imagery has a longer 16-day revisit interval, we have selected a longer time period for analysis. The daily Landsat-8 imagery is generated in a similar way as for other sensors: the TOA reflectances are corrected for Rayleigh scattering, the spatial resolution is enhanced using a panchromatic band, and the imagery is remapped in the geographical projection. The Landsat-8 OLI spectral bands used to

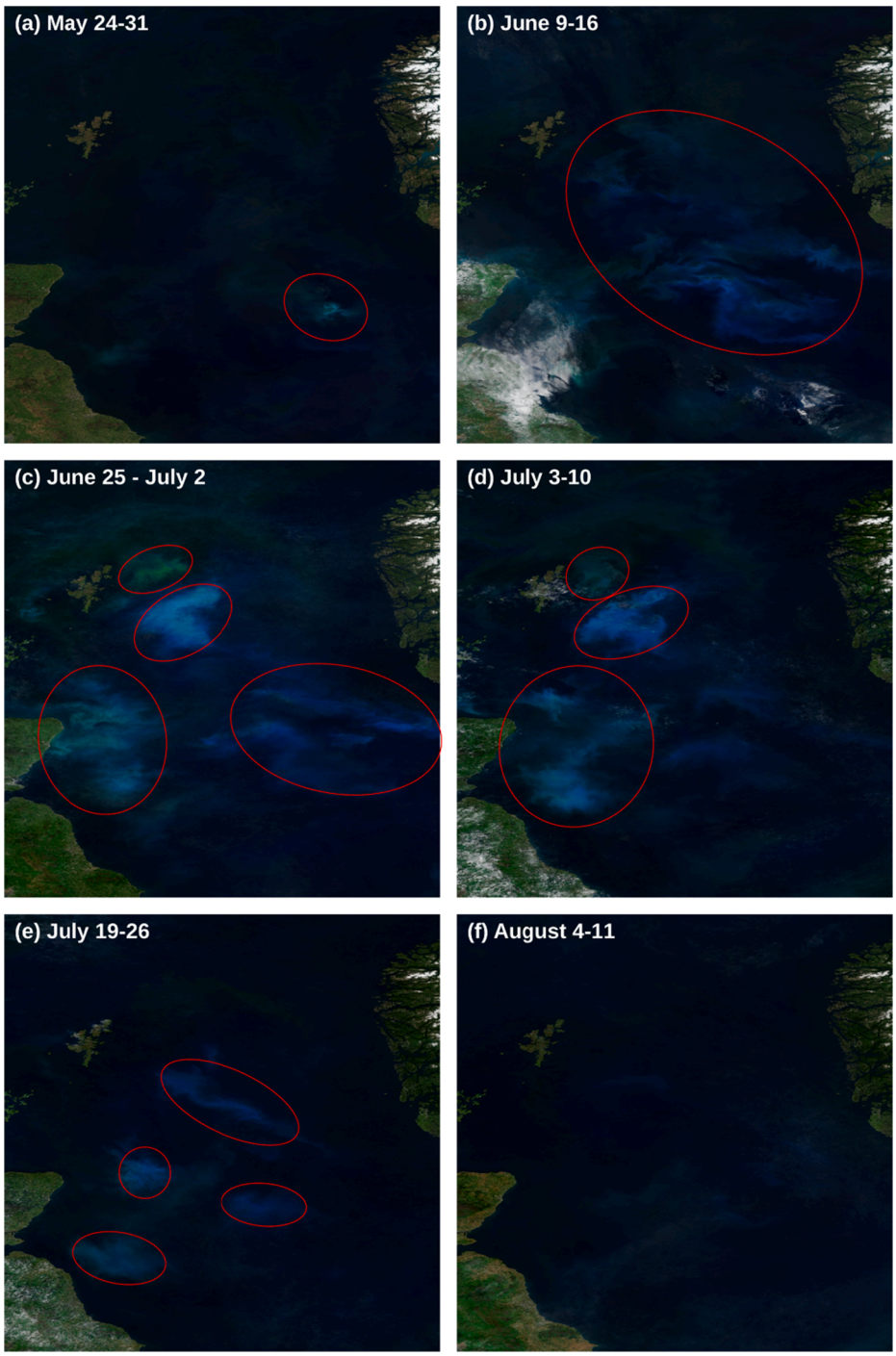

Fig. 12. Evolution of algae blooms (some marked with red ellipses) in the North Sea in summer 2020 using SARM from the 8-day average clear sky near-surface imageries of (a) May 24–31, (b) June 9–16, (c) June 25–July 2, (d) July 3–10, (e) July 19–26, and (f) August 4–11, which were derived from two VIIRS and two OLCI sensor daily imageries. (For interpretation of the references to color in this figure legend, the reader is referred to the web version of this article.)

produce the daily near-surface imagery using the proposed SARM are listed in Table 1. We did not use the quality assessment band flags, as we wanted to include partially cloudy scenes in the analysis. In this example, due to extreme cloudiness of the target area, we used all daily Landsat-8 scenes over this location from 2013 to 2020, with 166 scenes in total. However, since this is one of the most consistently cloudy locations on the planet, most of the scenes are either completely or nearly completely obscured by clouds. In Fig. 15, we show the three daily Landsat-8 scenes with the least cloud cover for this location (Fig. 15a–c), and provide the clear sky near-surface imagery derived from all 166 scenes using the new SARM (Fig. 15d), which show no clouds. The cloud shadows, more prevalent in high spatial resolution imagery, are also mostly avoided in the derived clear sky near-surface imagery. It is also evident that the clear sky near-surface imagery favors the darker green vegetation from the wet season (Fig. 15c) over the lighter scenes from the dry season (Fig. 15b). We note that this location represents one of the most difficult (most consistently cloudy) cases, thus most other locations are expected to produce even better results using shorter time series as input data.

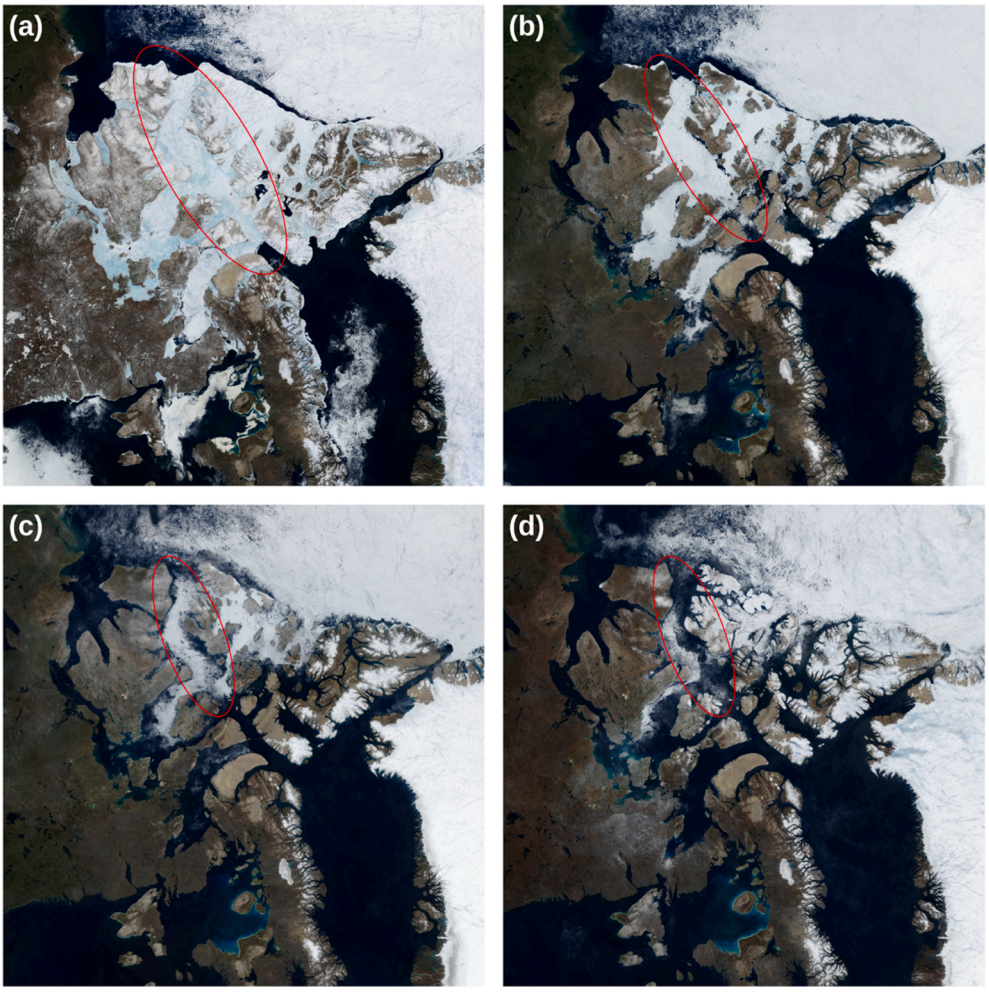

Fig. 13. Shrinking ice coverage in Canadian Arctic during summer 2019 in monthly clear sky near-surface imagery for the month of (a) June, (b) July, (c) August, and (d) September. Only patches of ice remained in the Northwest Passage (indicated by red ellipses) in September 2019. (For interpretation of the references to color in this figure legend, the reader is referred to the web version of this article.)

4. Discussion

We have developed a new method, i.e., SARM, to derive the clear sky near-surface imagery using multiple satellite-measured TOA reflectance data, and demonstrated various applications over global and regional scales. However, the new method introduced in this work is still subject to limitations, e.g., areas that are persistently covered by clouds will still remain cloudy in the clear sky near-surface imagery. Thus, it may be impossible to eliminate the clouds completely over short time averages, while longer time averages may fail to capture the rapid changes on the land and water surface. We note that any method faces a tradeoff between improving the temporal resolution and minimizing the effects of clouds and cloud shadows.

While in this work we have demonstrated applications of clear sky near-surface imagery using polar orbiting satellite sensor data, the proposed SARM can also be applied to derive clear sky near-surface imagery from the geostationary satellite data. In fact, increased observation frequency is expected to improve the statistics. However, it is not likely to avoid large and slow moving (relative to their size) cloud systems. Examples of clear sky near-surface imagery using the SARM from the geostationary satellite measurements, the Geostationary Ocean Color Imager (GOCI) onboard the Korean Communication, Ocean and Meteorological Satellite (COMS) (Cho et al., 2010; Choi et al., 2012; Wang et al., 2013a), are provided in Supplementary Section S2.

As noted above, the clear sky near-surface imagery is derived based on the statistically robust estimate for the darkest sample in the series, while trying to minimize the effects of cloud shadows. It implies that for time periods that span changing surface conditions, the clear sky near-surface imagery is inherently biased towards the darker scenes. For the areas undergoing seasonal changes of vegetation, the clear sky near-surface imagery favors darker green vegetation and disfavors lighter dried-out scenes. Therefore, bare land with or without vegetation is usually favored over much brighter snow/ice cover, and darker seasonal waters are favored over the dry land or vegetation, especially if the false color imagery is used. While clear sky near-surface imagery may have many applications, these considerations should be recalled in each case to avoid biases in results and decisions derived from it.

While the SARM proposed in this work uses daily imagery over a certain time period, it does not explicitly use the information about the exact collection time of each sample, as proposed, for example, in the method by Gómez-Chova et al. (2017). We surmise that our proposed SARM can be improved by including this additional information in the analysis and retrieval of the clear sky near-surface color. Indeed, other recent image reconstruction methods by Zhang et al. (2020; 2021) employ spatio-temporal filtering combined with machine learning, and are designed not only to fill the gaps left by clouds and cloud shadows in the individual scenes, but also to provide the temporal evolution, which is useful for enhancing the high-resolution sensor imagery that typically has long revisit intervals. In contrast, SARM relies on imagery statistics derived from frequent revisits typical for medium resolution

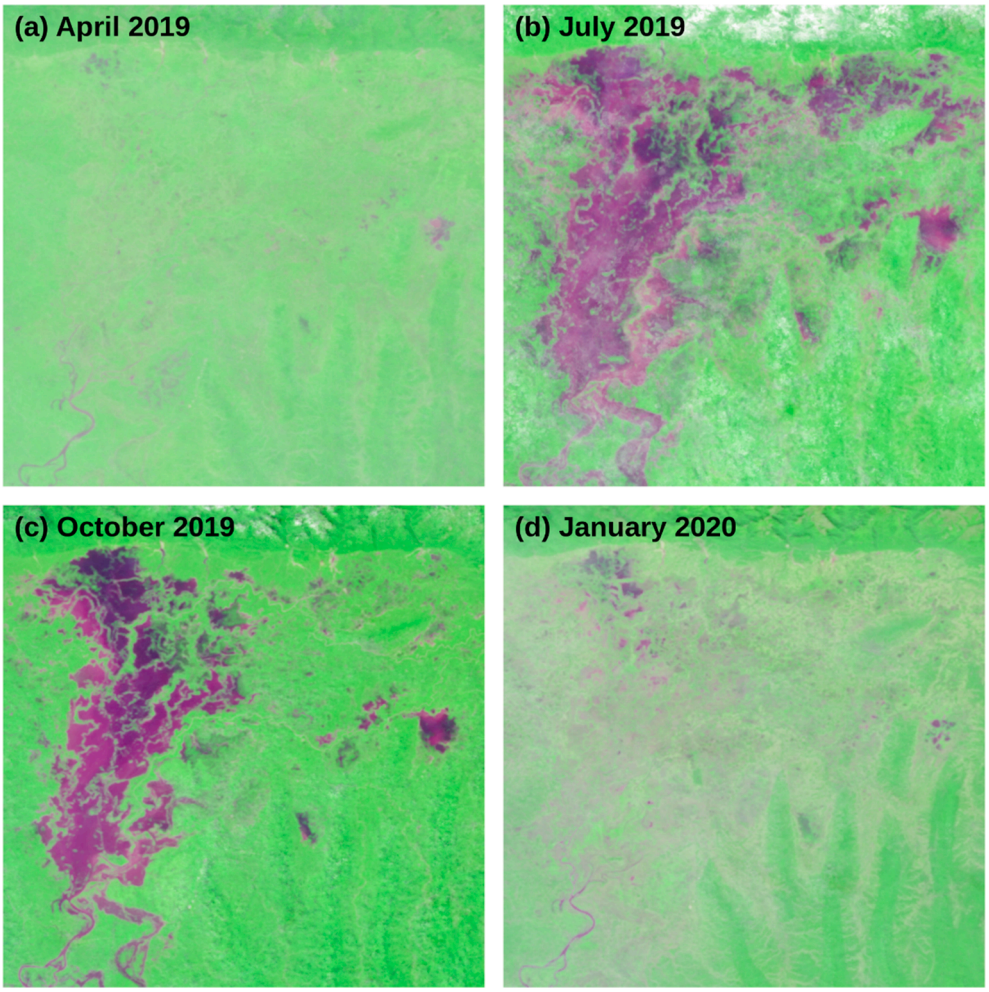

Fig. 14. Seasonal change in surface water extent in Bangladesh (150 × 150 km^2 scene with center at (24.6°N, 91.5°E)) in clear sky false color monthly imagery derived with SARM. Green color represents vegetation, and magenta implies surface water. (For interpretation of the references to color in this figure legend, the reader is referred to the web version of this article.)

environment monitoring sensors to derive a single representative clear sky-image. It also provides routine global clear-sky near-surface imagery efficiently. While most of the image reconstruction techniques rely on cloud and cloud shadow masking as a prerequisite step, the proposed SARM does not have this requirement. This can be advantageous if the cloud mask information is not readily available. To highlight the differences between SARM and other recently developed methods, we show an example application of SARM deriving clear-sky imagery from a few scenes of high-resolution Sentinel-2 data in Section S3 of the Supplemental Material.

The derivation of clear sky near-surface imagery is a computationally expensive task, as it involves mapping of all daily imagery. However, the daily global imagery from two VIIRS and two OLCI sensors is already routinely produced and displayed in OCView (Mikelsons and Wang, 2018). In addition, the mission-long daily global imagery time series for these four sensors are also available for display and analysis. Therefore, production of clear sky near-surface imagery from already existing mapped daily imagery comes at a relatively small additional computational cost, and provides a significant added value by aiding data visualization and interpretation.

Many applications of satellite imagery over land require imagery over specific and relatively small-scale target areas. For such cases, it is often possible to find specific high-resolution daily scenes that are completely free of clouds. Sequences of such scenes may be adequate for monitoring gradual changes over time, often due to human activities. However, most of the environmental monitoring over land, but especially over the oceans, requires imaging much larger areas to capture the relevant spatial length scales of the environmental changes. At these scales, it is very unlikely to find daily imagery that is free of clouds. At the same time, many of the environmental changes happen over relatively short time scales, particularly in the oceans where waters are subject to currents. All of these factors emphasize the importance of frequent global clear sky imagery for the global environmental data monitoring and interpretation.

5. Conclusions

We have proposed a new method (SARM) to produce clear sky near-surface imagery using the daily imagery scenes from multiple satellite sensors with frequent revisits, minimizing the effects of the clouds, dust, sun glint over water surfaces, and other conditions (or artifacts) present in daily imagery. We show how the correlation between the color saturation and brightness can be used to minimize the effects of cloud shadows. In addition, we have demonstrated the consistency, and improvements in quality of the derived clear sky near-surface imagery compared to simpler approaches, and shown several examples for applications for global, as well as regional land and water surface imaging. In the polar regions, the SARM can also be used to estimate the lowest extent of the sea ice over a particular time period. Likewise, over land in the polar regions, temperate and high-altitude regions, the new method

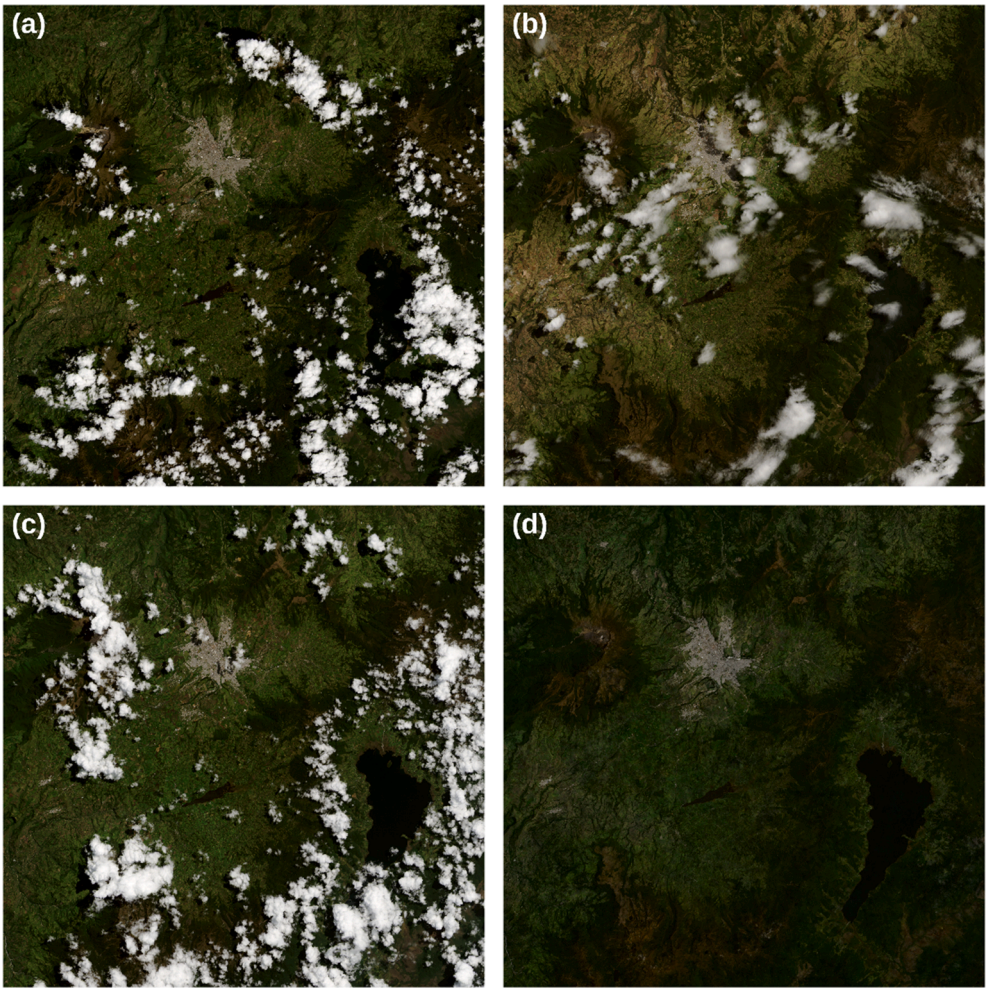

Fig. 15. The three least cloudy daily Landsat-8 scenes over 8 years of the mission (2013–2020) for (a) January 24, 2014, (b) August 25, 2016, and (c) April 22, 2017. The panel (d) is a clear sky near-surface imagery derived from Landsat-8 data over years 2013–2020 using the proposed SARM.

can also be used to estimate the lowest extent of the land snow and ice cover. In addition to the true color, the approach of SARM can be applied to false color imagery, making it especially useful in monitoring the extent of surface waters and vegetation. The method is also directly applicable to higher spatial resolution imagery, but may require the use of a series of images over longer time periods due to typically rarer revisits by high spatial resolution satellite sensors. In the age of increased public awareness about the state of the environment, the clear sky near-surface imagery represents a valuable visualization technique that makes environmental data more accessible and easier to interpret for a wider public with no need for a specialized expertise or even scientific background.

Declaration of Competing Interest

The authors declare that they have no known competing financial interests or personal relationships that could have appeared to influence the work reported in this paper.

Acknowledgments

This work was supported by the Joint Polar Satellite System (JPSS) funding. The Sentinel-3A/3B OLCI data were provided by ESA/EUMETSAT. The Landsat-8 OLI data were provided by USGS. The authors thank three anonymous reviewers for valuable comments and suggestions. The scientific results and conclusions, as well as any views or opinions expressed herein, are those of the authors and do not necessarily reflect those of NOAA or the Department of Commerce.

Appendix A. Supplementary material

Supplementary data to this article can be found online at https://doi.org/10.1016/j.isprsjprs.2021.08.013.

References

Ackerman, S.A., Strabala, K.I., Menzel, W.P., Frey, R.A., Moeller, C.C., Gumley, L.E., 1998. Discriminating clear sky from clouds with MODIS. J. Geophys. Res. 103, 32141–32157.

Benabdelkader, S., Melgani, F., 2008. Contextual spatiospectral postreconstruction of cloud-contaminated images. IEEE Geosci. Remote Sens. Lett. 5, 204–208.

Beurs, K.M.D., Henebry, G.M., 2004. Land surface phenology, climatic variation, and institutional change: Analyzing agricultural land cover change in Kazakhstan. Remote Sens. Environ. 89, 497–509.

Chen, B., Huang, B., Chen, L., Xu, B., 2017. Spatially and temporally weighted regression: A novel method to produce continuous cloud-free Landsat imagery. IEEE Trans. Geosci. Remote Sens. 55, 27–37.

Chen, S., Hu, C., Barnes, B.B., Xie, Y., Lin, G., Qiu, Z., 2019. Improving ocean color data coverage through machining learning. Remote Sens. Environ. 222–302, 286.

Cho, S., Ahn, Y.H., Ryu, J.H., Kang, G., Youn, H., 2010. Development of Geostationary Ocean Color Imager (GOCI). Korean J. Remote Sens. 26, 157–165.

Choi, J.K., Park, Y.J., Ahn, J.H., Lim, H.S., Eom, J., Ryu, J.H., 2012. GOCI, the world's first geostationary ocean color observation satellite, for the monitoring of temporal variability in coastal water turbidity. J. Geophys. Res. 117, C09004. https://doi.org/10.1029/2012JC008046.

Corbane, C., Politis, P., Kempeneers, P., Simonetti, D., Soille, P., Burger, A., Pesaresi, M., Sabo, F., Syrris, V., Kemper, T., 2020. A global cloud free pixel-based image

composite from Sentinel-2 data. Data in Brief 31, 105737. https://doi.org/10.1016/j.dib.2020.105737.
Cox, C., Munk, W., 1954. Measurements of the roughness of the sea surface from photographs of the sun's glitter. Jour. Opt. Soc. of Am. 44, 838–850.
Defries, R.S., Townshend, J.R., 2007. NDVI-derived land cover classifications at a global scale. Int. J. Remote Sens. 15, 3567–3586.
Donlon, C., Berruti, B., Buongiorno, A., Ferreira, M.-H., Féménias, P., Frerick, J., Goryl, P., Klein, U., Laur, H., Mavrocordatos, C., Nieke, J., Rebhan, H., Seitz, B., Stroede, J., Sciarra, R., et al., 2012. The global monitoring for environment and security (GMES) Sentinel-3 mission. Remote Sens. Environ. 120, 37–57. https://doi.org/10.1016/j.rse.2011.07.024.
Frantz, D., Röder, A., Udelhoven, T., Schmidt, M., 2015. Enhancing the detectability of clouds and their shadows in multitemporal dryland Landsat imagery: Extending Fmask. IEEE Geosci. Remote Sens. Lett. 12, 1242–1246.
Goldberg, M.D., Kilcoyne, H., Cikanek, H., Mehta, A., 2013. Joint Polar Satellite System: The United States next generation civilian polar-orbiting environmental satellite system. J. Geophys. Res. Atmos. 118, 13463–13475. https://doi.org/10.1002/2013JD020389.
Gómez-Chova, L., Amorós-López, J., Mateo-Garcia, G., Muñoz-Marí, J., Camps-Valls, G., 2017. Cloud masking and removal in remote sensing image time series. J. Appl. Remote Sens. 11, 015005. https://doi.org/10.1117/1.JRS.11.015005.
Hu, C., Lee, Z., Franz, B.A., 2012. Chlorophyll a algorithms for oligotrophic oceans: A novel approach based on three-band reflectance difference. J. Geophys. Res. 117, C01011 doi:01010.01029/02011JC007395.
Hu, G., Li, X., Liang, D., 2015. Thin cloud removal from remote sensing images using multidirectional dual tree complex wavelet transform and transfer least square support vector regression. J. Appl. Remote Sens. 9, 095053. https://doi.org/10.1117/1.JRS.9.095053.
Hughes, M.J., Hayes, D.J., 2014. Automated Detection of Cloud and Cloud Shadow in Single-Date Landsat Imagery Using Neural Networks and Spatial Post-Processing. Remote Sensing 6, 4907–4926. https://doi.org/10.3390/rs6064907.
IOCCG, 2010. Atmospheric Correction for Remotely-Sensed Ocean-Colour Products. In: Wang, M. (Ed.), Reports of the International Ocean-Colour Coordinating Group. IOCCG, Dartmouth, Canada. https://doi.org/10.25607/OBP-101.
Jiang, L., Wang, M., 2013. Identification of pixels with stray light and cloud shadow contaminations in the satellite ocean color data processing. Appl. Opt. 52, 6757–6770.
King, M.D., Platnick, S., Menzel, W.P., Ackerman, S.A., Hubanks, P.A., 2013. Spatial and temporal distribution of clouds observed by MODIS onboard the Terra and Aqua satellites. IEEE Trans. Geosci. Remote Sens. 51, 3826–3852.
Lee, Z.P., Carder, K.L., Arnone, R.A., 2002. Deriving inherent optical properties from water color: a multiple quasi-analytical algorithm for optically deep waters. Appl. Opt. 41, 5755–5772.
Lin, C., Tsai, P., Lai, K., Chen, J., 2013. Cloud removal from multitemporal satellite images using information cloning. IEEE Trans. Geosci. Remote Sens. 51, 232–241.
Liu, X., Wang, M., 2019. Filling the gaps of missing data in the merged VIIRS SNPP/NOAA-20 ocean color product using the DINEOF method. Remote Sens. 11, 178. https://doi.org/10.3390/rs11020178.
Mateo-Garcia, G., Gómez-Chova, L., Amorós-López, J., Muñoz-Marí, J., Camps-Valls, G., 2018. Multitemporal cloud masking in the Google Earth Engine. Remote Sens. 10, 1079. https://doi.org/10.3390/rs10071079.
Melgani, F., 2006. Contextual reconstruction of cloud-contaminated multitemporal multispectral images. IEEE Trans. Geosci. Remote Sens. 44, 442–455.
Mikelsons, K., Wang, M., 2018. Interactive online maps make satellite ocean data accessible. Eos Trans. AGU 99. https://doi.org/10.1029/2018EO096563.
Mikelsons, K., Wang, M., Jiang, L., 2020. Statistical evaluation of satellite ocean color data retrievals. Remote Sens. Environ. 237, 111601. https://doi.org/10.1016/j.rse.2019.111601.
O'Reilly, J.E., Werdell, P.J., 2019. Chlorophyll algorithms for ocean color sensors - OC4, OC5 & OC6. Remote Sens. Environ. 229, 32–47.
Qi, L., Hu, C., Mikelsons, K., Wang, M., Lance, V., Sun, S., Barnes, B.B., Zhao, J., Zande, D.V., 2020. In search of floating algae and other organisms in global oceans and lakes. Remote Sens. Environ. 239, 111659. https://doi.org/10.1016/j.rse.2020.111659.
Roy, D.P., Wulder, M.A., Loveland, T.R., Woodcock, C.E., Allen, R.G., Anderson, M.C., Helder, D., Irons, J.R., Johnson, D.M., Kennedy, R., Scambos, T.A., Schaaf, C.B., Schott, J.R., Sheng, Y., Vermote, E.F., Belward, A.S., Bindschadler, R., Cohen, W.B., Gao, F., Hipple, J.D., Hostert, P., Huntington, J., Justice, C.O., Kilic, A., Kovalskyy, V., Lee, Z.P., Lymburner, L., Masek, J.G., McCorkel, J., Shuai, Y., Trezza, R., Vogelmann, J., Wynne, R.H., Zhu, Z., 2014. Landsat-8: Science and product vision for terrestrial global change research. Remote Sens. Environ. 145, 154–172.
Salomonson, V.V., Barnes, W.L., Maymon, P.W., Montgomery, H.E., Ostrow, H., 1989. MODIS: advanced facility instrument for studies of the Earth as a system. IEEE Trans. Geosci. Remote Sens. 27, 145–153.
Scaramuzza, P.L., Bouchard, M.A., Dwyer, J.L., 2012. Development of the Landsat data continuity mission cloud-cover assessment algorithms. IEEE Trans. Geosci. Remote Sens. 50, 1140–1154.
Sen, P.K., 1968. Estimates of teh regression coefficient based on Kendall's tau. J. Am. Statistical Assoc. 63, 1379–1389.
Sharma, R.C., Hara, K., Tateishi, R., 2017. High-resolution vegetation mapping in Japan by combining Sentinel-2 and Landsat 8 based multi-temporal datasets through machine learning and cross-validation approach. Land 6, 50. https://doi.org/10.33990/land6030050.
Shi, W., Wang, M., 2019. A blended inherent optical property algorithm for global satellite ocean color observations. Limnol. Oceanogr. Methods 17, 377–394. https://doi.org/10.1002/lom3.10320.
Shi, W., Wang, M., Jiang, L., 2011. Spring-neap tidal effects on satellite ocean color observations in the Bohai Sea, Yellow Sea, and East China Sea. J. Geophys. Res. 116, C12032. https://doi.org/10.1029/2010JC007234.
Shi, W., Wang, M., Jiang, L., 2013. Tidal effects on ecosystem variability in the Chesapeake Bay from MODIS-Aqua. Remote Sens. Environ. 138, 65–76. https://doi.org/10.1016/j.rse.2013.07.002.
Stock, A., Subramaniam, A., Dijken, G., Wedding, L., Arrigo, K., Mills, M., Cameron, M., Micheli, F., 2020. Comparison of cloud-filling algorithms for marine satellite data. Remote Sens. 12, 3313. https://doi.org/10.3390/rs12203313.
Theil, H., 1950. A rank-invariant method of linear and polynomial regression analysis. Nederlandse Akademie Wetenchappen Series A 53, 386–392.
Wang, M., Ahn, J.H., Jiang, L., Shi, W., Son, S., Park, Y.J., Ryu, J.H., 2013a. Ocean color products from the Korean Geostationary Ocean Color Imager (GOCI). Opt. Express 21, 3835–3849. https://doi.org/10.1364/OE.21.003835.
Wang, M., Bailey, S., 2001. Correction of the sun glint contamination on the SeaWiFS ocean and atmosphere products. Appl. Opt. 40, 4790–4798.
Wang, M., Liu, X., Tan, L., Jiang, L., Son, S., Shi, W., Rausch, K., Voss, K., 2013b. Impact of VIIRS SDR performance on ocean color products. J. Geophys. Res. Atmos. 118, 10347–10360. https://doi.org/10.1002/jgrd.50793.
Wang, M., Shi, W., 2006. Cloud masking for ocean color data processing in the coastal regions. IEEE Trans. Geosci. Remote Sens. 44, 3196–3205. https://doi.org/10.1109/tgrs.2006.876293.
Wang, M., Son, S., 2016. VIIRS-derived chlorophyll-a using the ocean color index method. Remote Sens. Environ. 182, 141–149. https://doi.org/10.1016/j.rse.2016.05.001.
Wang, M., Son, S., Harding Jr., L.W., 2009. Retrieval of diffuse attenuation coefficient in the Chesapeake Bay and turbid ocean regions for satellite ocean color applications. J. Geophys. Res. 114, C10011. https://doi.org/10.1029/2009JC005286.
Xu, M., Jia, X., Pickering, M., Jia, S., 2019. Thin cloud removal from optical remote sensing images using the noise-adjusted principal components transform. ISPRS J. Photogramm. Remote Sens. 149, 215–225.
Zhang, Q., Yuan, Q., Li, J., Li, Z., Shen, H., Zhang, L., 2020. Thick cloud and cloud shadow removal in multitemporal imagery using progressively spatio-temporal patch group deep learning. ISPRS J. Photogramm. Remote Sens. 162, 148–160.
Zhang, Q., Yuan, Q., Li, Z., Sun, F., Zhang, L., 2021. Combined deep prior with low-rank tensor SVD for thick cloud removal in multitemporal images. ISPRS J. Photogramm. Remote Sens. 177, 161–173. https://doi.org/10.1016/j.isprsjprs.2021.04.021.
Zhang, Q., Yuan, Q., Zeng, C., Li, X., Wei, Y., 2018. Missing data reconstruction in remote sensing image with a unified spatial-temporal-spectral deep convolutional neural network. IEEE Trans. Geosci. Remote Sens. 56, 4274–4288.
Zhu, X., Gao, G., Liu, D., Chen, J., 2012. A modified neighborhood similar pixel interpolator approach for removing thick clouds in Landsat images. IEEE Geosci. Remote Sens. Lett. 9, 521–525.
Zhu, Z., Wang, S., Woodcock, C.E., 2015. Improvement and expansion of the Fmask algorithm: Cloud, cloud shadow, and snow detection for Landsats 4–7, 8, and Sentinel 2 images. Remote Sens. Environ. 159, 269–277.
Zhu, Z., Woodcock, C.E., 2012. Object-based cloud and cloud shadow detection in Landsat imagery. Remote Sens. Environ. 118, 83–94.